SEARCH FOR COHERENT X-RAY PULSATIONS FROM NEUTRON STARS IN LOW MASS X-RAY BINARIES USING ROSSI X-RAY TIMING EXPLORER OBSERVATIONS

by
YUNUS EMRE BAHAR

Submitted to the Graduate School of Engineering and Natural Sciences
in partial fulfillment of the requirements for the degree of
Master of Science

Sabancı University
JULY 2020

SEARCH FOR COHERENT X-RAY PULSATIONS FROM NEUTRON STARS IN LOW MASS X-RAY BINARIES USING ROSSI X-RAY TIMING EXPLORER OBSERVATIONS

Approved by:

Prof. Dr. Ersin Göğüş ....
(Thesis Supervisor)

Prof. Dr. Ünal Ertan ....

Prof. Dr. Kazım Yavuz Ekşi ....

Date of Approval:

06/07/2020

ABSTRACT

SEARCH FOR COHERENT X-RAY PULSATIONS FROM NEUTRON STARS IN LOW MASS X-RAY BINARIES USING ROSSI X-RAY TIMING EXPLORER OBSERVATIONS

YUNUS EMRE BAHAR

PHSYICS, M.SC. THESIS, JULY 2020

Thesis Supervisor: Prof. Dr. Ersin Göğüş

Keywords: low mass X-ray binaries, neutron stars, X-rays, timing analysis

Low mass X-ray binaries (LMXBs) are binary systems that emit luminous X-rays mainly by converting the gravitational energy of the matter from a low mass (M $\lesssim$1 $M_{\odot}$) star into radiation as it accretes onto a neutron star or a black hole. Only a small fraction of LMXBs show coherent pulsations during their persistent emission phase. The cause of the lack of pulsations is still unclear. Detection of intermittent pulsations from a few LMXBs promise a better understanding of the physical mechanism causing the absence of pulsations. In this thesis, we present the results of our extensive search for pulsations in 13 LMXBs after binary orbital motion correction. These selected sources exhibit burst oscillations in X-rays with frequencies ranging from 45 to 1122 Hz, and have a binary orbital period varying from 2.1 to 18.9 hours. We first determined episodes that contain weak pulsations around the burst oscillation frequency by searching all archival Rossi X-ray Timing Explorer (RXTE) data of these sources. Then, we applied binary orbital corrections to these pulsation episodes to discard the smearing effect of the binary orbital motion and searched for recovered pulsations at the second stage. Here we report 75 pulsation episodes that contain weak but coherent pulsations around the burst oscillation frequency. Furthermore, we report eight new episodes that show relatively strong pulsations in the binary orbital motion corrected data. We also present results of our two sets of simulations: one is to understand the effects of orbital binary motion to the pulse detection and the other one is to find the relation between pulsed the fractional amplitude and source intensity.

ÖZET

DÜŞÜK KÜTLELİ X-IŞINI ÇİFTLERİNDEKİ NÖTRON YILDIZLARINDAN GELEN PERİYODİK ATMALARIN ROSSI X-RAY TIMING EXPLORER GÖZLERİMLERİNDE ARANMASI

YUNUS EMRE BAHAR

FİZİK YÜKSEK LİSANS TEZİ, TEMMUZ 2020

Tez Danışmanı: Prof. Dr. Ersin Göğüş

Anahtar Kelimeler: düşük kütleli X-ışını çiftleri, nötron yıldızları, X-ışınları, zamanlama analizi

Düşük kütleli X-ışını çiftleri (LMXB), düşük kütleli (M $\lesssim$1 M$_\odot$) bir yıldızdaki maddenin kütle çekimsel enerjisinin bir nötron yıldızı veya karadeliğe akarken radyasyona dönüştürülmesiyle parlak X-ışını yayan ikili sistemlerdir. Bu sistemlerin sadece küçük bir kısmı devamlı ışıma yaptıkları evrede eş fazlı periyodik atmalar gösterir ve bunun nedeni bilinmemektedir. LMXB'lerden gelen birkaç geçici peryodik atmanın tespit edilmesi bu atmaların gözlemlenememesine sebep olan fiziksel mekanizmanın daha iyi anlaşılmasını vaat eder. Bu tezde, 13 düşük kütleli X-ışını çifti verisine ikili yörünge düzeltmesi uyguladıktan sonra yaptığımız periyodik atma aramamızın sonuçlarını sunuyoruz. Seçilen bu kaynaklar, 45 ila 1122 Hz arasında değişen frekanslarda X-ışını patlama salınımları gösterir ve 2.1 ila 18.9 saat arasında değişen bir ikili yörünge periyodunda sahiptir. İlk olarak bu kaynakların arşivlenmiş tüm Rossi X-ray Timing Explorer (RXTE) verilerini araştırarak patlama salınım frekansı etrafında zayıf atmalar içeren bölümler belirledik. Daha sonra, ikili yörünge hareketinin dağıtma etkisini ortadan kaldırmak için atma içeren bölümlere ikili yörünge düzeltmeleri uyguladık ve ardından kurtarılmış atmalar aradık. Salınım frekansı çevresinde zayıf fakat düzenli atmalar içeren 75 atma bölümü bildiriyoruz. Bununla birlikte, ikili yörünge hareketi etkisi düzeltilmiş verilerde sekiz yeni atma bölgesi rapor ediyoruz. Ayrıca biri, ikili yörünge hareketinin atma belirlenmesi üzerine etkisini anlamak ve diğeri, kaynak ışıma şiddeti ile fraksiyonel atma genliği arasındaki bağlantıyı bulmak üzere olan iki simülasyon gurubunun sonuçlarını sunuyoruz.

ACKNOWLEDGEMENTS

I express my gratitude to my advisor Prof. Ersin Göğüş for his support and guidance along the way. We had a lot of fruitful discussions that were occasionally a bit bitter; all of those took my academic vision one step further and helped me to achieve my goals. I am thankful for the remarkable time and effort he spent on guiding and helping me in any circumstance.

I also would like to thank Prof. M. Ali Alpar and Prof. Nihat Berker for their support and guidance for me to carry on my career in physics. Their encouragement helped me a lot to find my path throughout my journey.

I acknowledge support from the Scientific and Technological Research Council of Turkey (TÜBİTAK, grant no: 115R034).

I thank Ebrar for her love, understanding, and support. None would be possible without her.

Last but not least, I thank my family, Meral, Mehmet, and Sina, for their continuous support and encouragement on becoming who I want to be. I always feel their love and support that help me a lot to overcome obstacles in my life.

TABLE OF CONTENTS

LIST OF TABLES

LIST OF FIGURES

LIST OF ABBREVIATIONS

AMXP: accreting millisecond X-ray pulsar

ASM: All Sky-Monitor

BT: Blandford & Teukolsky

FFT: fast Fourier transform

FWHM: full width at half maximum

HEXTE: High Energy Timing Experiment

LMXB: low mass X-ray binary

NICER: Neutron Star Interior Composition Explorer

PCA: Proportional Counter Array

PCU: Proportional Counter Unit

QPO: quasi-periodic oscillation

RXTE: Rossi X-ray Timing Explorer

1. INTRODUCTION

In this thesis, I present our study of neutron stars in low mass X-ray binaries (LMXBs). We focused on searching coherent pulsations in the X-ray observations of EXO 0748–676, IGR J17191–2821, 4U 1702-429, 4U 1728-34, KS 1731-260, A 1744-361, Aql X–1, MXB 1658-298, 4U 1636-536, SAX J1750.8-2900, GS 1826-238, 4U 1608-52, XTE 1739-285 sources and aimed to better understand the reason behind the lack of coherent pulsations in the persistent emission of most of the LMXBs. In this chapter, I briefly introduce neutron star, LMXBs and I explain some of the physical phenomena that takes place in these systems and relevant to our investigations.

1.1 Neutron Stars

Neutron stars are compact objects that can form from the energetic explosions called supernova. These explosions occur either when a massive star collapse to itself due to the imbalance between the gravitational pull and radiation pressure or when a white dwarf with mass near the critical level detonates due to external mass transfer. The latter leaves nothing behind, while in the former case, a neutron star or a black hole might emerge. The dramatic collapse in the former case makes these objects quite extreme in the terms of their densities, magnetic field strengths and spin periods (Miller & Miller, 2015). Neutron stars typically have a mass of ~ 1.4 $M_\odot$ and a radius of ~ 10 km which gives a typical average density of $\sim 10^{14}$ g cm^{-3} that is about the nuclear density (Özel & Freire, 2016). They can have magnetic field strengths up to 10^{15} G due to the conservation of magnetic flux of the collapsing star. Moreover, compactness of the neutron stars require them to have very short spin periods (down to 10^{-3} s) due to the conservation of angular momentum. These extreme properties that arise from fundamental laws make these objects attracting to study in many fields of physics.

Early theoretical predictions of neutron stars were made by Landau (1932) right after the discovery of neutron by Chadwick (1932). The discovery of neutron stars dates back to 1965 by Jocelyn Bell and her supervisor Anthony Hewish (Hewish et al., 1968). Bell recognized coherent periodicities while working on radio observations of quasars which later found out to be coming from the radio pulsar CP 1919. Their discovery pawed the way for Hewish to receive the Nobel Prize in 1974. Later studies of these objects revealed their emission in X-ray and γ-ray bands which further increased the interest to these objects and led the discovery of many more.

1.2 Neutron Stars in Low Mass X-ray Binaries

Most of the stars in the universe are not isolated but in binaries. Binary star systems are structures where two stars are gravitationally bound to each other. The two objects revolve around the common center of mass to form stable orbits and not fall onto each other. If the companion star in such systems has a mass $\lesssim 1$ M$_\odot$ and is transferring matter onto a compact object (i.e., a neutron star), it results in bright X-ray emission, and the system is called low mass X-ray binary (LMXB). LMXBs are typically old ($\sim 1-10$ Gyr), tend to have lower magnetic fields ($\sim 10^8-10^{11}$ G) compared their younger relatives and powered by the gravitational energy of the accreting matter onto the compact object (Harding, 2013).

Matter transfer in these systems takes place when the companion star fills its Roche-lobe, that is the hypothetical region for the matter to be gravitationally bound to the star. Roche-lobe filled star starts accreting matter onto the compact object through the inner Lagrangian point. Transferred material cannot fall directly onto the compact object because of its angular momentum. Instead, it forms an accretion disk, in which matter looses angular momentum, spirals in, and eventually be transferred onto the compact object. See Fig 1.1 for the artist's impression of an accretion disk in a LMXB. Gravitational energy is converted to kinetic energy during this spiral fall that heats the accretion disk. Inner regions of the accretion disk can reach at temperatures up to 10^7 K which correspond to a black body spectrum that peaks around a few keV (see section 1.3 of Frank et al., 2002). These energies correspond to the energies of X-ray photons which makes the disk to emit X-rays and be bright in this band. Accretion disks of LMXBs can get very close to the neutron star surface because of the low magnetic fields that is less capable to stop and channel the matter contrary to the younger neutron stars with higher magnetic fields. The region where the accretion meets with the neutron star is called the boundary layer. In this layer, the matter gets close to the neutron star such that it starts being effected by the magnetic field, neutron star surface and the physical structure and composition close to the surface. Interaction of the hot accretion matter with the physical environment close to the surface also generate energetic X-ray photons which adds one more component to the total emission of the LMXB that is called boundary layer emission (Popham & Sunyaev, 2001). Boundary layer region is complex due to the transition of the accreting matter in the disk to the neutron star surface in extreme physical conditions. Chaotic accretion through this region to the neutron star surface is still a highly investigated phenomenon and I present my observational work on the pulse generation problem of this phenomenon in this thesis.

1.2.1 Accretion Theory

Accretion onto compact objects (in our case neutron stars) is a complex process. However, general properties and of the accretion disk and the dynamical processes taking place in it can be understood by the standard model (Shakura & Sunyaev, 1973). Matter of the companion star has large amount of potential energy when it passes through the inner Lagrangian point. If the gas could convert all of its gravitational potential energy into radiation, the accretion luminosity would be $L_{acc} = GM\dot{M}/R_*$, where G is the universal gravitational constant, M is the mass of the compact object, $\dot{M}$ is the mass accretion rate, and R_* is the radius of the compact object. If we assume the falling matter to be mostly ionized hydrogen, then we can obtain an upper limit to the luminosity from a stable object by equating inbound (gravitational) and outbound (radiation pressure) forces acting on the electron proton pairs. The limit is called Eddington luminosity (L_{Edd}) and formulated as:

$$L_{Edd} = \frac{4\pi G M m_p c}{\sigma_T} \cong 1.3 \times 10^{38} (M/M_\odot)\ erg\ s^{-1} \tag{1.1}$$

where m_p, c, σ_T are mass of proton, speed of light, electron Thomson cross-section for scattering, respectively (see Frank et al. (2002) for a simple derivation).

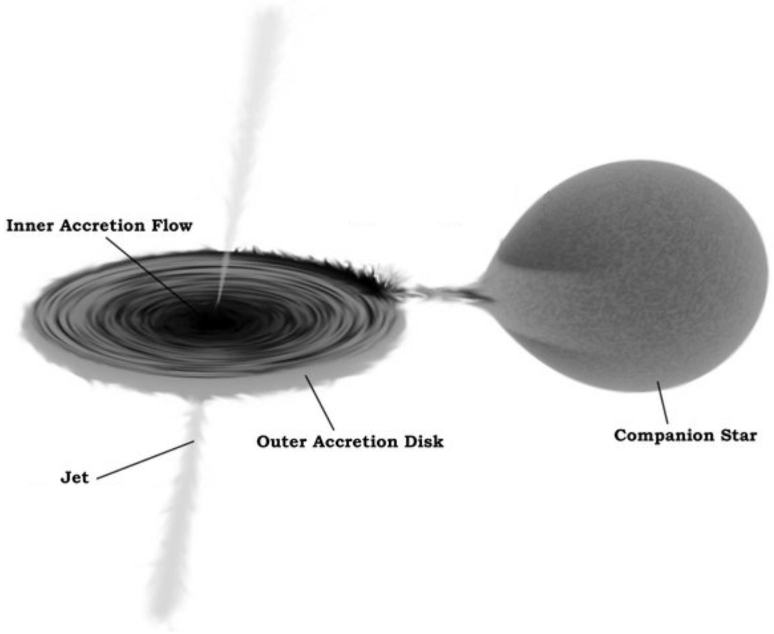

Figure 1.1 Artists impression of a low mass X-ray binary. Figure is taken from Hynes (2010)

For the purpose of this thesis I will focus on the standard accretion theory onto LMXBs, which was developed by Shakura & Sunyaev (1973). In their model, they assumed that the radial extension of the disk to be much greater than scale height ($H/R << 1$) which make the disk to be optically thick but geometrically thin. In this model, particles in the disk are assumed to be in virial equilibrium and the accreting matter rotating around the neutron star to have a Keplerian angular velocity of $\Omega_K = \sqrt{GM/R^3}$. Also, energy dissipation in the disk is assumed to be due to viscous processes which cause the angular momentum to be transferred outwards. Viscosity in this model is famously known as "α-prescription" and it is defined as $\nu = \alpha c_s H$ where α is the free kinematic viscosity parameter and c_s is the speed of sound.

Temperature of the disk varies radially because of this viscous processes. In a Newtonian treatment, half of the total accretion energy will be dissipated in the disk and the other half is going to be converted to energy in the boundary layer. With the use of that, radial dependence of the effective temperature among the radial direction for the disk becomes $T_{eff} \propto R^{-3/4}$. This relation assumes that the disk only heats up due to viscous dissipation however, temperature profile should be modified if irradiation of the disk by the neutron star emission is taken into account. It dominates over T_{eff} at larger radii and goes as $T_{irr} \propto R^{-1/2}$. In any case, temperature of the disk differs along the radial direction and this make the total spectrum of the disk to be sum of blackbodies which is also called a multi-coloured blackbody (Bhattacharyya et al., 2000).

Accretion disk of many LMXBs oscillate between two states namely quiescence and outburst. Transition from quiescence to outburst state takes place when the gas temperature becomes sufficiently high to ionize hydrogen. This transition can start at any part of the disk where the temperature exceeds a critical temperature of ~ 6500 K due to temperature fluctuations. These fluctuations cause viscous stress at that part of the disk to increase because of the temperature dependence of viscosity in alpha prescription. Increased viscosity results in the environment to heat up and cause a runaway effect that ionize the neighbouring gas. Eventually all the disk becomes ionized due to so called hydrogen instability (Done et al., 2007). The source is dimmer, colder and less viscous in the quiescence state, whereas it becomes brighter, hotter and more viscous after transiting to the outburst state. After some time, outer skirts of the disk gets colder and hydrogen starts to recombine. This cooling front moves inward until all the gas in the disk become neutral. This makes the disk to get back to quiescence state and the whole cycle repeats.

The region where the magnetic field lines dominantly determine the flow of the accreting gas is called magnetosphere. This region starts at a radius called magnetospheric radius (r_m) where the magnetic stresses are equal to the material stresses in the disk. There is another distance measure called Alfvén radius (r_A) where the kinetic energy density becomes equal to the magnetic energy density. Alfvén radius can be formulated as

$$r_A = \left(\frac{\mu^4}{2GM\dot{M}^2}\right)^{1/7} \tag{1.2}$$

where μ is the magnetic moment of the neutron star (Ghosh & Lamb, 1979). Assuming the neutron star as a solid sphere, the magnetic dipole moment will be

$$\mu = B_p {R_*}^3 \tag{1.3}$$

where B_p is the magnetic field intensity at the magnetic pole. Alfven radius and the magnetospheric radius are close to each other and their relation can be expressed as $r_m = \xi r_A$ where ξ is the dimensionless parameter ($\xi \sim 1$).

Keplerian velocity of the accreting gas increases as the matter gets closer to the neutron star surface. Along the radial direction, there is a hypothetical point where the angular velocity of the neutron star becomes equal to the angular Keplerian gas

Table 1.1 Alfvén radii estimates of investigated sources

Source	L_{peak}/L_{Edd}	r_A (km)	References
EXO 0748–676	0.033*	20.7	1
4U 1702-429	0.033†	21.1	2
4U 1728-34	0.09†	15.8	2
KS 1731-260	0.1§	15.6	3
A 1744-361	0.15*	13.5	1
Aql X–1	0.45*	9.83	1
MXB 1658-298	0.08*	16.1	1
4U 1636-536	0.1†	15.3	2
SAX J1750.8-2900[a]	0.09†	15.8	4
GS 1826-238	0.11*	14.7	1
4U 1608-52	0.32*	10.8	1

References. — 1. Wu et al. (2010); 2. Yu & Yan (2009); 3. Šimon (2012); 4. Tang et al. (2011)

Notes. — Peak luminosities of XTE 1739-285 and IGR J17191–2821 were not present in the literature either due to unknown distance or lack of studies for these sources. We assumed mass, radius and magnetic field of the neutron star to be 1.4 $M_\odot$, 10 km and 10^8 G respectively for calculating r_A.

[a] Luminosity of a bright outburst phase is used instead of peak luminosity because of the lack of information about the peak luminosity of the source in the literature.

[*] Peak luminosities are reported for 3-200 keV and we assumed L_{peak} to be 80% of L_{bol} for this energy band.

[†] Peak luminosities are reported for 2-12 keV and we assumed L_{peak} to be 85% of L_{bol} for this energy band.

[§] Peak luminosities are reported for 1-10 keV and we assumed L_{peak} to be 90% of L_{bol} for this energy band.

velocity in the case where there is no magnetic interruption. This radius is called co-rotation radius and it is formulated as

$$r_{co} = \left(\frac{GM}{\Omega^2}\right)^{1/3} \tag{1.4}$$

where Ω is the angular velocity of the neutron star. With a canonical approach, if the accreting matter is interrupted by the magnetic field at the magnetospheric radius (r_m) before the co-rotation radius (r_{co}) then it slows down the neutron star by removing angular momentum. Furthermore, if the accreting matter can reach to the co-rotation radius without any magnetic interruption then it speeds up the neutron star by contributing additional angular momentum. For convenience, we provide estimated Alfvén radii of the sources investigated in this work in Table 1.1.

1.2.2 Oscillations

Most of the LMXBs do not exhibit coherent pulsations in their X-ray data. The systems that show pulsations are called accreting millisecond X-ray pulsars (AMXPs). AMXPs were theoretically predicted as a link between millisecond radio pulsars and LMXBs by Alpar et al. (1982). It took about 16 years to confirm this prediction by the detection of the first AMXP (Wijnands & van der Klis, 1998). In a broader sense, there are three types of oscillations observed from LMXBs: coherent and long term pulsations, quasi-periodic oscillations and thermonuclear burst oscillations (see Bhattacharyya, 2009). All three are the manifestations of different mechanisms, therefore, reveal different characteristics of the LMXB.

1.2.2.1 Coherent Periodicities

Coherent and long term X-ray pulsations from LMXBs are thought to originate from the hot spot at the polar caps of the neutron star. Weak magnetic fields could still channel the inflowing gas to these regions where the kinetic energy of the accreting matter is converted to X-ray emission. This adds a modulated component to the total emission due to the miss alignment of the polar caps with the spin axis. This scenario is not fully confirmed and we still are not sure why only a small portion of the LMXBs show these pulsations. However, we are confident that the pulsations are coming from the surface which reveal the spin frequency of the neutron star (Patruno & Watts, 2012). See Figure 1.2 for an example of the power spectrum and pulse profile of a coherent pulsation coming from an AMXP.

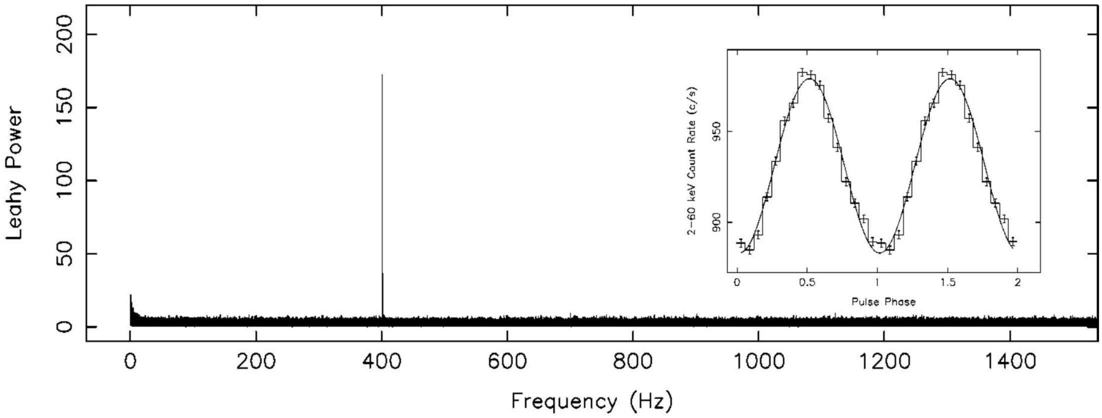

Figure 1.2 Typical power spectrum of a coherent pulsation from an accreting millisecond X-ray pulsar (SAX J1808.4-3658; first discovered AMXP). Figure is taken from van der Klis (2000)

1.2.2.2 Quasi-periodic Oscillations

Besides coherent pulsations, LMXBs also show oscillations that contain signal power in a broader frequency range that are called quasi-periodic oscillations (QPOs). Central frequencies of QPOs are observed in many different frequency regimes ranging from milli Hertz to kilo Hertz. QPO frequency is known to be related with the place of the source in the color-color diagram (van der Klis, 2006). However, the origin of QPOs is still an unsolved and highly investigated problem. Along with all the uncertainty about the origin of these oscillations, QPOs at higher frequencies (kHz QPOs) are thought to be coming from the inner regions of the accretion disk since outer parts of the disk is slow to show periodicities at such high frequencies. An example of the power spectrum of a twin kHz QPO can be seen in Figure 1.3.

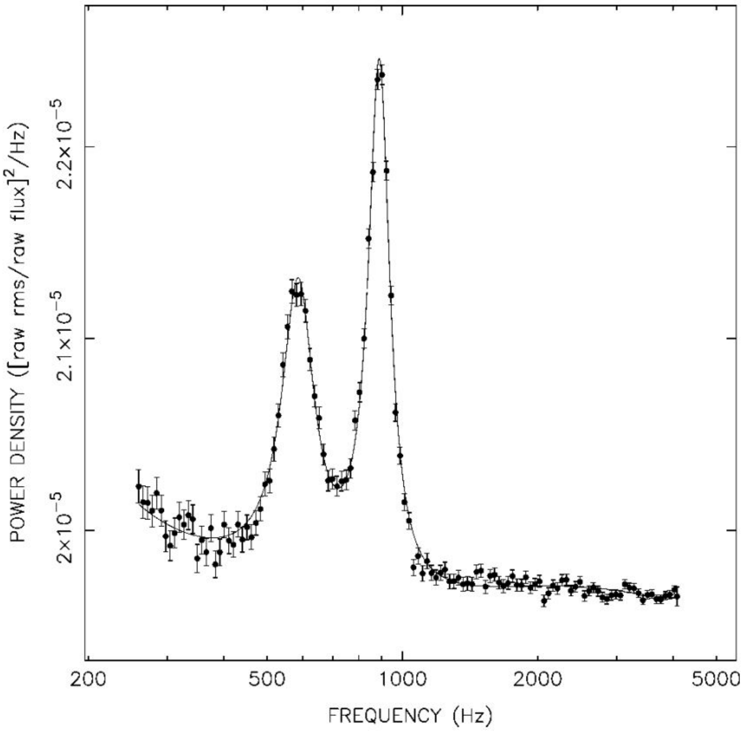

Figure 1.3 Power spectrum of a twin kHz QPO from Sco X-1. Figure is taken from van der Klis et al. (1997)

1.2.2.3 Thermonuclear Burst Oscillations

Thermonuclear X-ray bursts are dramatic increase and usually subsequent exponential decay of the X-ray flux seen only from LMXBs containing neutron stars (Strohmayer & Bildsten, 2006; Watts, 2012). Also called Type I X-ray bursts, their source of energy is the fusion of H coming from the accreting stream into He. Burst profiles may contain oscillations whose period is very close to the neutron star spin period. This shows that, thermonuclear fusion takes place at the surface while resulting a temporary hot spot (Strohmayer et al., 1996). Frequency of the oscillation usually slowly change with time during the bursts which indicates the hot spot is moving or spreading on the neutron star surface. After the sharp increase, X-ray flux drops gradually and the source gets back to the level before the event. Bursts typically have a $\sim 1-2$ s rise time before the peak and $\sim 10-1000$ s decay time. The amount of energy released at such short times shows that the matter needed to be accumulated before the ignition and the reaction is unstable (Strohmayer & Bildsten, 2006). Gravitational energy per baryon is ~ 200 MeV wheres nuclear fusion of hydrogen can only generate ~ 5 MeV which would be lost in the total emission if there was no sudden burn of the accumulated matter (Bildsten, 2000). Examples of Type I X-ray burst profiles with the underlying burst oscillations, whose frequency is varying, can be seen in Figure 1.4.

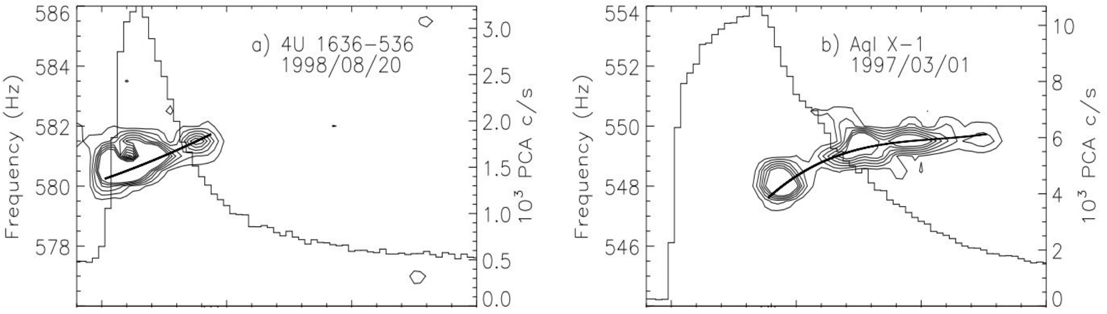

Figure 1.4 Frequency evolution and burst profile of two burst oscillations observed from 4U 1636–536 and Aql X–1. Figure is taken from Muno et al. (2002)

1.2.3 Lack of Pulsations

Accreting millisecond X-ray pulsars has emerged as a subclass of neutron stars in LMXBs in the last two decades (Patruno & Watts, 2012). These transient systems exhibit coherent pulsations with periods shorter than ∼10 ms. The remarkable capability of AMXPs to turn the accretion energy into pulsations raises a question regarding the reason behind the lack of X-ray pulsations from the majority of the LMXBs. There might be no emerging pulsations from majority of LMXBs possibly because of insufficient magnetic field strengths to canalize the accreting matter to the magnetic pole. Alternatively, the beamed signal could already be present but weak; it might be further weakened to non-detection while emerging pulsed radiation undergoes various dynamical or physical processes. Detection of intermittent episodes of coherent pulsations in the persistent emission phase from couple of systems (Aql X–1, Casella et al. (2008); SAX J1748.9–2021, Altamirano et al. (2008)) support the case that all neutron stars in LMXBs are likely to radiate X-ray pulse. These observations provided a unique opportunity to better understand the reason of appearance and then disappearance of the pulsed emission.

There are various neutron star atmosphere and surroundings effects that can reduce the pulse amplitude, and in turn, lead to the lack of pulsations. The most notable scenarios for this situation include light bending effect resulting from the extreme gravity of the compact object (Wood et al., 1988; Özel, 2009), nearly aligned magnetic and spin axes (Lamb et al., 2009a,b), scattering characteristics of the environment surrounding the neutron star (Brainerd & Lamb, 1987; Titarchuk et al., 2002), and the magnetohydrodynamic instabilities in the accretion flow (Kulkarni & Romanova, 2008). Another possible cause is the binary orbital motion, which could smear the already weak signal to non-detection. Such a dynamical effect would introduce significant implications on the pulsed signal especially in tight binary systems. In such systems, it could, in principle, be possible to recover a pulsed signal in the X-ray data if the binary orbital effects are accounted for.

1.2.3.1 Orbital Effects and Pulse Smearing

Physical mechanism behind pulse smearing is the relativistic Doppler effects caused by the rotational motion of the neutron star around the common center of mass of the binary system. Effectively, Doppler effects modulate the signal by causing delays on the photon arrival times depending on the relative position of the neutron star on its orbit. This delay was formulated by Blandford & Teukolsky (1976) for observing and testing various relativistic effects by making use of the information that pulsars are reliable and precise clocks. See Section 2.3.2 for the details of the formulation. In this study, we use this formulation to revert the effect of the binary orbital motion to possibly strengthen the pulsed signal.

There have been several extensive studies to correct smearing of pulsations due to dynamical effects from binary neutron stars. One approach, the acceleration search provides a partial correction by splitting the data into short segments and assuming that the orbital acceleration of the neutron star to be approximately constant during the segments of the binary orbit which corresponds to the exposure time of the obsevation (e.g. Middleditch & Kristian, 1984; Anderson et al., 1990; Wood et al., 1991). Later, Ransom et al. (2001, 2002) elaborated this technique to obtain template responses in the frequency - frequency derivative (f-$\dot{f}$) plane. They correlate the Fourier amplitude and phase responses of the real time data with template responses that are generated with trial acceleration values. Recently, it was extended by assuming jerk ($\ddot{f}$) to be constant, instead of the orbital acceleration (Andersen & Ransom, 2018). By doing that they added one more dimension to their parameter space and conducted their search in f-$\dot{f}$-$\ddot{f}$ volume which they called jerk search (Andersen & Ransom, 2018). These methods are widely employed to search for periodic signal in timing data collected in the radio band.

Another approach to detect smeared pulsations is called semi-coherent search. It was first proposed as a technique to detect weak gravitational wave signals (Messenger, 2011), and then applied to search for weak X-ray signals from neutron stars in LMXBs (Messenger & Patruno, 2015; Patruno et al., 2018). The focus of this method is to detect weak but continuous pulsations. They attempted to achieve this goal by applying a two-step procedure on the X-ray data. In the first stage, they divide data to segments and process each segment with a bank of templates coherently. These templates are produced such that they account for the Doppler modulation in the phase of the signal by a Taylor expansion in frequency. In the second stage they incoherently combine the coherent signal power results obtained for each segment. They applied this technique to 12 LMXBs and no evidence was found for a previously non-detected weak pulsation.

Note that both strategies to search for weak pulsations relied on a template based pulse profile modelling. However, in this work we aim to avoid the smearing effect by transforming the photon arrival times to an inertial frame at the common center of mass of the binary system from the moving neutron star frame.

2. INSTRUMENTATION AND TIMING TECHNIQUES

2.1 Rossi X-ray Timing Explorer

We have performed our investigations based on the data collected by Rossi X-ray Timing Explorer (RXTE). It was launched on 30^{th} of December in 1995 and completed its mission on 5^{th} January in 2012. It had an initial goal of 5 years of operation. Nevertheless, it was able to conduct observations for ∼16 years. It operated in a low-earth circular orbit that was 580 km away from the Earth and had three science instruments installed on the spacecraft, namely, High Energy X-ray Timing Experiment (HEXTE), All Sky-Monitor (ASM) and Proportional Counter Array (PCA) which are labeled in Fig 2.1.

All Sky-Monitor was made up of three wide-angle detectors that was operating at $2-10$ keV (Levine et al., 1996). 6500 square cm. It was capable of scanning 80 % of the sky in 90 minutes with its detectors having 0.125 s time resolution.High Energy X-ray Timing Experiment was made up of two clusters of four scintillation detectors (Rothschild et al., 1998). Its total collecting area was 1600 cm^2 and was operating at a wide energy range of $15-250$ keV. Detectors had a time resolution of 8 μs, a field of view of 1° FWHM and energy resolution of 15 % at 60 keV. Each cluster was capable of providing background measurements 1.5 or 3.0 degrees away from the source by oscillating ("rock") in orthogonal directions every 16 to 128 s.

Proportional Counter Array was made up of 5 Proportional Counter Units (PCUs) that were nearly identical and operating at $2-60$ keV (Jahoda et al., 1996). All of our data employed here are collected with the PCA. Its total collecting area was 6500 cm^2 and had a a field of view of 1° FWHM. Detectors had an energy resolution of < 18 % at 6 keV and a time resolution of ~ 1 μs. There were 256 energy channels spanning in the $2-60$ keV energy range. However, its response has slightly changed during the lifetime of RXTE due to propane loss in some PCUs. For this reason 5 epochs are considered and different energy response schemes are assigned to channels in different epochs. It should be noted that high time resolution is the most important feature of PCA for our work here due to the fact that time scales around neutron stars are very short.

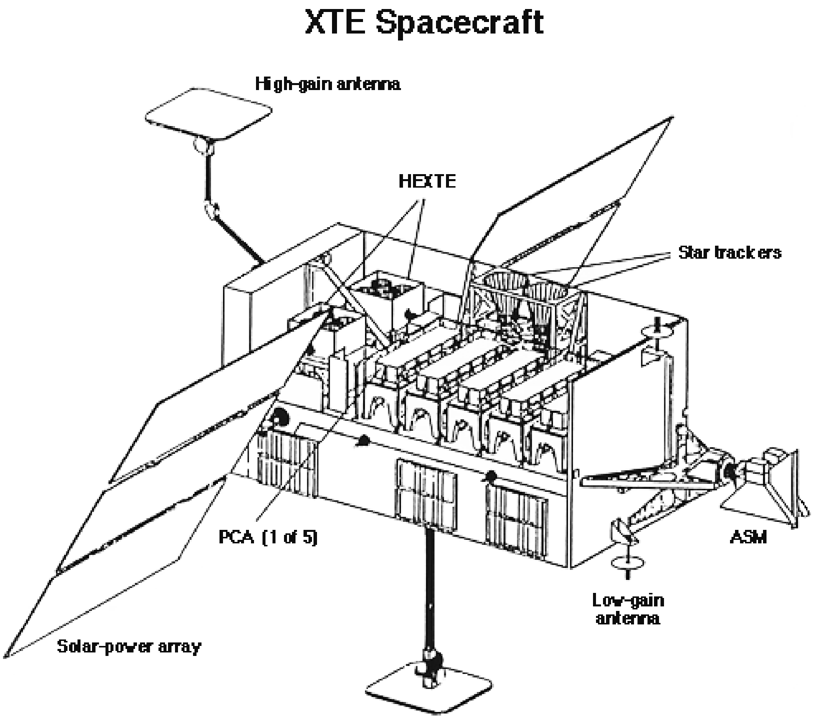

Figure 2.1 Diagram of Rossi X-ray Timing Explorer and its three instruments PCA, HEXTE and ASM (labeled). Image is taken from https://heasarc.gsfc.nasa.gov/Images/xte/xte_spacecraft.gif

2.2 Timing Analysis

X-ray observations of neutron stars in binaries contain a great deal of information about the neutron star and the structure of the binary. These binaries embody considerable amount of events and structures that leave timing signatures in X-ray, such as the spin of the neutron star and the binary orbital motion, because of their relatively short time scale periodic nature. In many fields of science, signals that contain periodicities are studied by a well established technique called Fourier transform that converts the time domain information into frequency domain. X-ray data being discrete results in a more specific technique to be used called discrete Fourier transform to analyze it. Assuming the signal to be a series of equally spaced

N many numbers, discrete Fourier transform decomposes the signal into N sine waves where the weight of each wave is represented by a Fourier amplitude (a_j). Complete transformation that is responsible of the conversion between time and frequency domains consists of two formulas that are formulated as

$$\begin{aligned} a_j &= \sum_{k=0}^{N-1} x_k e^{2\pi ijk/N} && j = \frac{N}{2}, .., \frac{N}{2} - 1 \\ x_k &= \frac{1}{N} \sum_{k=-N/2}^{N/2-1} a_j e^{-2\pi ijk/N} && k = 0, .., N-1 \end{aligned} \tag{2.1}$$

where x_k is the value of the k'th time series. Furthermore, if the length of the signal is T then the frequency of the sinusoidal that a_j corresponds to can be found as $\omega_j = 2\pi j/T$.

In our work, we mainly used two timing techniques that are related with discrete Fourier transform to unveil coherent pulsations from LMXBs namely Leahy normalized power spectrum (Leahy et al., 1983) and Z^2 statistic (Buccheri et al., 1983). For the scope of this work only these techniques are discussed in this thesis. See van der Klis (1988) for a more complete and detailed guide on X-ray timing analysis.

2.2.1 Leahy Normalized Power Spectrum

Discrete power spectrum is the modulus square of the Fourier amplitudes. It can be normalized in various ways to achieve different statistical characteristics. Leahy normalization is one of these normalization choice that provide the noise powers to be distributed as χ^2 with 2 degrees of freedom and the mean of the powers to be 2. In order to apply the normalization one need to first compute the Fourier amplitudes of the signal (lightcurve) of interest. Thankfully, there is a very fast and convenient method for this purpose that is called fast fourier transform (FFT). FFT reduce the compexity of calculating Fourier amplitudes from $\mathcal{O}(N^2)$ to $\mathcal{O}(N \log(N))$ which results in significant decrease in the computation time. For a given Fourier amplitudes, Leahy normalized powers can be calculated as

$$P_j = \frac{2}{N_{ph}} |a_j|^2 \qquad j = 0, .., \frac{N}{2} \tag{2.2}$$

where P_j, N_{ph}, a_j, N are j'th Leahy normalized power, total number of photons, j'th Fourier amplitude and number of bins, respectively. It is one of the most commonly used technique in X-ray astronomy because of its easy implementation, short computation time and statistical properties. However, there is one downside of calculating Leahy normalized power spectrum; that is, it requires the data to be binned (i.e., a lightcurve) for the technique to be applicable.

2.2.2 Z^2 Statistic

Z^2 statistic is another commonly used method to detect pulsations. It is working principle is similar to the Fourier transform but the main advantage of this method is it does not require the photon arrivals to be binned. Another advantage of this method is that it provides an easy way of summing harmonics. Phase of the each photon (ϕ_j) is needed to be calculated in order to calculate the Z^2 powers. ϕ_j can be calculated as

$$\phi_j = 2\pi \int_{t_0}^{t_j} \nu(t) dt \tag{2.3}$$

where $\nu(t)$ is the frequency of interest, t_j is the photon arrival time and t_0 is a reference time. After calculating ϕ_j for each photon, Z^2 powers of the signal can be calculated as

$$Z_n^2 = \frac{2}{N} \sum_{m=1}^{n} [\{\sum_{j=1}^{N} \cos(m\phi_j)\}^2 + \{\sum_{j=1}^{N} \sin(m\phi_j)\}^2] \tag{2.4}$$

where n, N, ϕ_j are the number of harmonics, total number of photons and phase of the j^{th} photon. Z_n^2 powers are also distributed as χ^2 but with 2n degrees of freedom this time. In general, it is advantageous over Leahy normalized power spectrum since frequency in Z^2 statistic can be chosen to be variable with time and no information is lost by binning the data. However, high computation time of Z^2 statistic method is a major drawback.

For these reasons, I used Leahy normalized power spectrum when we were analyzing long observations. I used Z^2 statistic when more targeted but more detailed analysis was required.

2.3 Timing Corrections

Almost all satellites orbit around a celestial object to prevent them falling down. This require the satellites to rotate at short periods (~ 90 min for RXTE) and very high speeds (~ 8 km s^{-1} for RXTE) to stay in stable orbits. Moreover, neutron stars in LMXBs also rotate at relatively short periods ($\mathcal{O}(1)$ hr) around the common center of mass with their companion star. These two oscillatory motions and relativistic effects modify the photon arrival times. These modifications are needed to be corrected to study high precision timing. For that reason, I applied two timing corrections in our work namely: barycentric timing correction and binary orbital timing correction.

2.3.1 Barycentric Timing Correction

Barycentric correction is a modification applied to the photon arrival times to account for the orbital and relativistic effects acting on the data collecting satellite. RXTE revolved around the Earth which revolves around the Sun. Moreover, gravitational potential field of Earth and Sun also introduce some relativistic delays. Barycentric correction compensate these effects by effectively as if the satellite was placed into an inertial frame at the solar system barycenter from the moving satellite frame. Correction is applied to each photon individually by calculating appropriate delays between the non-inertial frame and the barycenter. It became a standard procedure for high precision timing studies since all satellites experience these delays that are needed to be corrected. See Taylor & Weisberg (1989) for a more comprehensive review of this correction.

2.3.2 Binary Orbital Timing Correction

Rotational motion of the neutron star around the common center of mass introduce additional delays to the photon arrival times. These delays can be corrected by applying appropriate binary orbital timing correction. In our work I used Blandford & Teukolsky (1976) relativistic orbit model to measure the delays. Blandford & Teukolsky (BT) delay was first formulated to test relativistic effects by using pulsars as reliable and precise clocks. However, in this work I used it to revert the Doppler effects on weak pulse signals. Similar to the barycentric correction, binary orbital timing correction effectively carry the photon arrival times from the moving neutron star frame to an inertial frame at the common center of mass. BT delay is formulated as

$$t_d = \{\alpha(\cos E - e) + (\beta + \gamma)\sin E\} \times \left\{1 - \frac{2\pi}{P_b}\frac{\beta\cos E - \alpha\sin E}{1 - e\cos E}\right\} \tag{2.5}$$

where x, α, β parameters are defined as

$$x = a\sin i, \quad \alpha = x\sin w, \quad \beta = \left(1 - e^2\right)^{1/2} x\cos w \tag{2.6}$$

and E, e, P_b, w, γ are eccentric anomaly, eccentricity, binary period, longitude of periastron and the term for gravitational redshift and time dilation respectively. Lastly, the eccentric anomaly is formulated as

$$E - e\sin E = \frac{2\pi t}{P_b} \tag{2.7}$$

which is the Kepler's equation (Taylor & Weisberg, 1989). In this work, I assumed the orbits to be circular ($e = 0$) that is a plausible approximation for LMXBs. With this assumption, number of free parameters drops to three which are the projected semi-major axis (x), binary orbital period (P_b) and the epoch of mean longitude equal to zero (T_0). An example power spectrum of a signal before and after BT binary orbital timing correction is applied can be found in Figure 2.2. It is evident from the figure that the binary orbital timing correction is effective to recover smeared signals due to orbital effects.

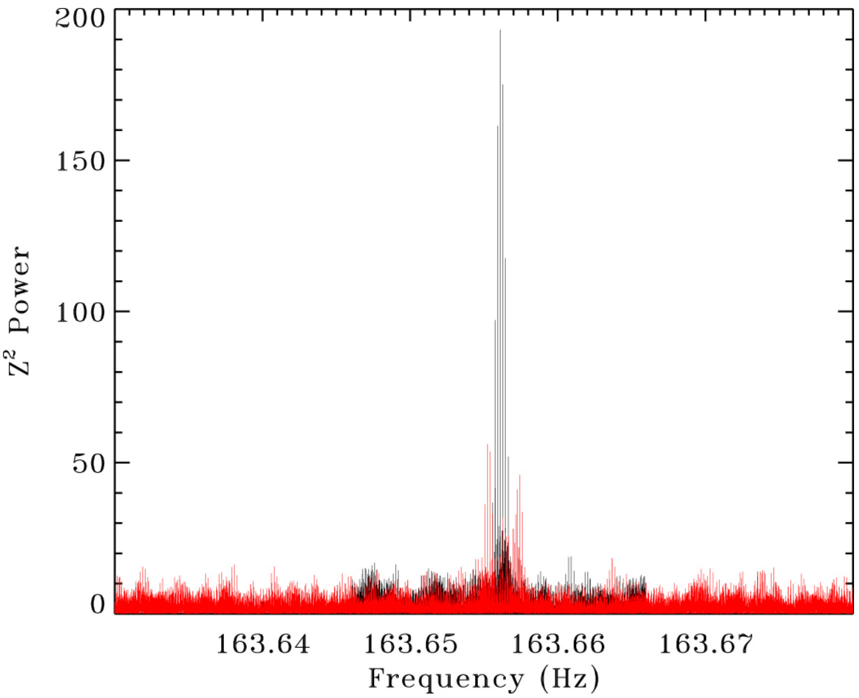

Figure 2.2 Power spectrums of the NICER observation of IGR J17062–6143 before (*red*) and after (*black*) binary orbital motion correction is applied. Figure is taken from Strohmayer et al. (2018)

3. OBSERVATIONS AND PULSATION SEARCH

We performed the search for weak pulsations in two steps. In the first tier, we conducted pulse search on the barycentered data and determined the candidates. In the second step, we applied arrival time corrections to these candidates to account for the effects of the binary motion and re-searched for pulsations in the corrected data.

3.1 Observations, the 1^{st} Tier Search and Results

For the first tier pulsation search, we selected 13 neutron star low mass X-ray binary and used all available event mode archival RXTE data. Note that none of these sources show X-ray pulsations above the noise level during their persistent emission phase (except Aql X–1). However, ten of them show prominent quasi-periodic oscillations just before, during or just after they ignite a thermonuclear X-ray burst. Remaining three also have reported periodicities in their burst observations. Nevertheless, these sources (XTE 1739–285, A 1744–361, GS 1826–238) show either only one burst or the burst oscillations are tentative. We assume that thermonuclear burst oscillations correspond to an X-ray emitting hotspot and the spin frequency of the underlying source is around the frequency of these oscillations (see Watts (2012)). Binary orbital periods of six of these sources are known either from periodicities or eclipses observed in the X-ray data. We present the list of the sources investigated and their burst oscillation frequencies in Table 3.1.

Before applying the first tier search, we generated the light curve of each RXTE pointing in the 2–60 keV energy band with 0.125 s time resolution to search for thermonuclear X-ray bursts. We then created good time intervals for each source by excluding the times of identified X-ray bursts. In particular, we excluded the data starting 20 seconds before the burst peak till 200 seconds after. This conservative

Table 3.1 Fundamental characteristics and RXTE observational details of the systems investigated

Source	f_s (Hz)	P_b (Hr)	Average Count Rate ($counts\ s^{-1}\ PCU^{-1}$)[b]	t_{tot} (ks)	References
EXO 0748–676	45/552[a]	3.82	38.4	2228.5	1, 2
IGR J17191–2821	294	...	113.4	82.9	3
4U 1702-429	329	...	141.3	1250.4	4
4U 1728-34	363	...	287.8	1649.3	5
KS 1731-260	524	...	155.0	468.9	6, 7
A 1744-361	530	...	140.2	117.7	8
Aql X–1	550	18.95	368.0	1646.6	9, 10, 11, 12
MXB 1658-298	567	7.11	73.9	339.0	13
4U 1636-536	581	3.80	248.0	4384.7	14, 15
SAX J1750.8-2900	601	...	179.6	214.7	16, 17
GS 1826-238	611	2.10	124.6	1012.4	18
4U 1608-52	620	12.89	349.1	2113.2	17, 19, 20
XTE 1739-285	1122	...	91.5	118.9	21

References. — 1. Villarreal & Strohmayer (2004); 2. Galloway et al. (2010); 3. Altamirano et al. (2010); 4. Markwardt et al. (1999); 5. Strohmayer et al. (1996); 6. Smith et al. (1997); 7. Muno et al. (2000); 8. Bhattacharyya et al. (2006); 9. Chevalier & Ilovaisky (1991); 10. Zhang et al. (1998); 11. Welsh et al. (2000); 12. Casella et al. (2008); 13. Wijnands et al. (2001); 14. Strohmayer et al. (1998); 15. Strohmayer & Markwardt (2002); 16. Kaaret et al. (2007); 17. Galloway et al. (2008); 18. Thompson et al. (2005); 19. Hartman et al. (2003); 20. Wachter et al. (2002); 21. Kaaret et al. (2007)

Abrreviations — f_s: Burst Oscillation Frequency; P_b: Orbital Period; t_{tot}: Total Time

[a] There are two different burst oscillation frequencies reported for EXO 0748–676.

[b] Average count rates are calculated in the energy range of ~3-27 keV from the all available X-ray data excluding thermonuclear bursts, that is, segment from 20 s before till 200 s after the peak of X-ray bursts.

selection excludes any possible contribution from even the relatively longer duration bursts. Note that the source 4U 1728–34 has a type-II X-ray burster (the Rapid Burster) in its RXTE PCA field of view. For this system, we ignored all observations with type-II bursts present and excluded them from our list of good time intervals. We list the total investigated observing time for each source after the exclusion of the burst intervals in Table 3.1. Finally, we transferred the photon arrival times to the Solar System barycenter to get rid of the relativistic effects of the moving frame of the detector.

In the first tier search, we fixed channel ranges from one observation to the other rather than fixing energy ranges because energy-channel relation of RXTE has changed during its lifetime. This did not create any problem since we have not compared any observation to the other directly. We applied statistical analysis techniques for comparing any result to the other.

To make our search sensitive for the pulsations that are made up of only hard or low energy X-ray photons, we carried out the first step of our pulsation search in three energy bands; ∼3-9 keV (absolute channels of 7-24), ∼9-27 keV (channel range of 25-70), and ∼3-27 keV (7-70 channels). Here we note that the energy ranges may vary slightly between the various gain epochs as we have kept the channel range fixed. For each energy band, we constructed a 256 second window at the very beginning of each observation and generated a lightcurve from the photons that are within this window with a 1/2048 s binning. This bin size corresponds to a maximum frequency of 1024 Hz in the Fourier domain and it is above all of the reported LMXB burst oscillation frequencies except XTE 1739–285 for which we used 1/4096 s binning. We constructed the Leahy normalized power density spectrum (Leahy et al., 1983) from this lightcurve and calculated the statistical significance of the maximum power between $f_s \pm 10$ Hz where f_s is the reported burst oscillation frequency. This is done by first determining the highest Leahy power between $f_s \pm 10$ Hz. The frequency range is chosen as such because the frequency shift observed during burst oscillations is conservatively of this order (Watts, 2012) and therefore the deviation of the oscillation frequency from the spin frequency is expected in this range. Then the single trial probability of obtaining the highest Leahy power is found and joint probability of having the spectrum is calculated with the number of trials (N_{trials}) equal to the number of frequency bins between $f_s \pm 10$ Hz. At last, significance level of this joint probability is calculated from a normal distribution in the light of the central limit theorem. We then slided the 256 s interval by 16 seconds, repeated the same procedure to obtain the significance for that time interval, and continued until the end of the observation. This procedure would facilitate the detection and strengthening of any signal which is present of a short time duration.

After calculating the statistical significance of the strongest pulse for each window, we selected candidates by applying the following continuity, coherence and minimum significance criterion. We require a pulsation candidate for further detailed analysis to have at least 2.5σ statistical significance for four consecutive time segments and having the maximum Leahy power between $f_s \pm 2$ Hz. By setting this criterion we aimed to uncover coherent periodicities around the burst oscillation frequency that are just below the detection threshold. Our first tier search resulted in 75 episodes of pulsation candidates from 10 sources. We also found that the search in the broader energy range resulted in the same pulsation candidates in the lower and upper energy bands. We, therefore, continued our investigations within the absolute channel range of 7 to 70 (∼3 - 27 keV).

Conventional fast Fourier transform (FFT) can only be applied to discrete data with equally spaced time axis. For that reason, photon arrival times are binned and histograms are created to apply FFT. Even though this approach is computationally very effective, it also has downsides. To be able to bin the data one need to choose the starting time of the binning according to the first photon of interest. Power spectrum may slightly change depending on the choice of the starting time of the binning because shifting the starting and ending times of the histogram bins can cause the photons to be redistributed which will change the values of the histogram. For these reasons, we confirmed the pulsation candidates by using a Z^2 test (Buccheri et al., 1983) which is computationally more expansive but it does not require the data to be binned. See Section 2.2.2 for the details and the formulation of Z^2 powers and test.

We have chosen the number of harmonics to be 1 for calculating Z^2 powers since strong harmonics are not reported for the sources of interest. The Z^2 powers are calculated with a 1/512 Hz frequency resolution between $f_s \pm 2$ Hz. Significance values are calculated with the same approach as above. We present the results of our first tier search and the corresponding pulsation candidates in Table 3.2. For each LMXB we present an example pulsation episode in Figures 3.1 to 3.10. Pulsation episodes corresponding to these figures are indicated in boldface in Table 3.2. As in these cases, none of our candidate pulsation episodes contain burst emission.

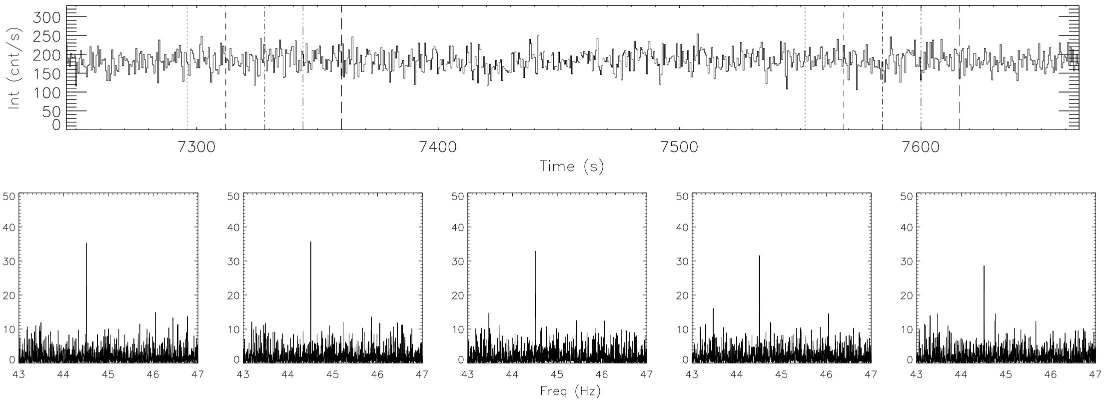

Figure 3.1 Example of a candidate pulsation episode that is displayed for five consecutive time windows. The source of this pulsation candidate is EXO 0748–676, and starting time is 1998 Mar 14 01:02:04.9. *(top panel)* The light curve of the part of the observation that contains 320 s long candidate pulsation episode. The vertical dashed lines that have the same line style correspond to the starting and ending time of 256 s windows from which power spectra are calculated. *(bottom plots)* Z^2 power density spectra of the five sequential 256 s intervals indicated with vertical lines above. The signal at 44.51 Hz is clearly evident in all plots.

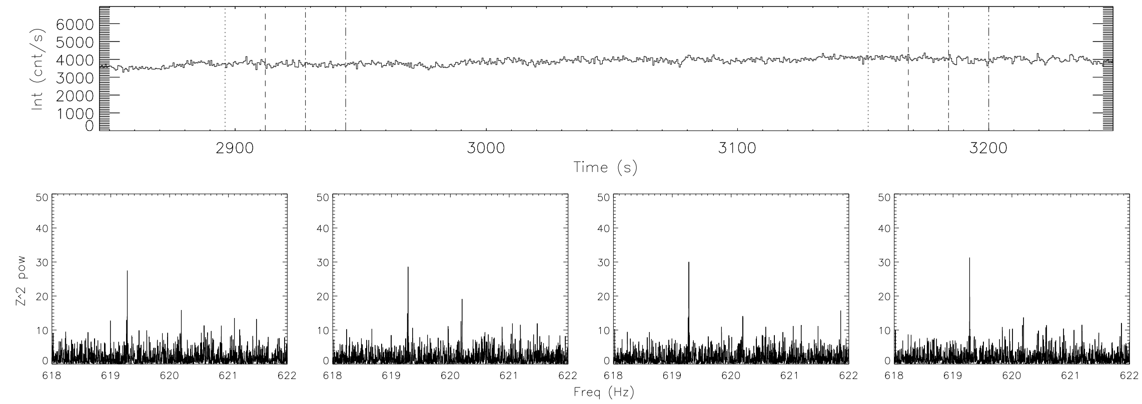

Figure 3.2 Example of a candidate pulsation episode that is displayed for four consecutive time windows. The source of this pulsation candidate is 4U 1608—52, and starting time is 2007 Nov 1 06:39:10.1. *(top panel)* The light curve of the part of the observation that contains 304 s long candidate pulsation episode. The vertical dashed lines that have the same line style correspond to the starting and ending time of 256 s windows from which power spectra are calculated. *(bottom plots)* Z^2 power density spectra of the four sequential 256 s intervals indicated with vertical lines above. The signal at 619.28 Hz is clearly evident in all plots.

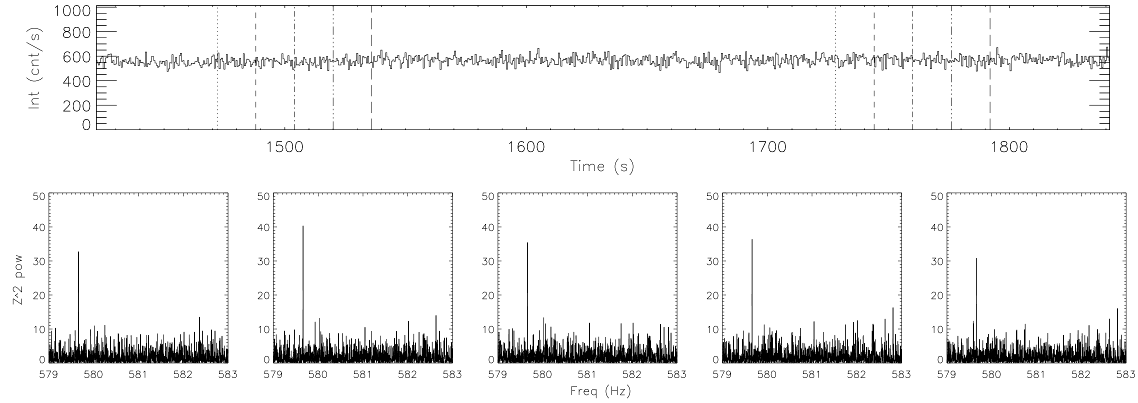

Figure 3.3 Example of a candidate pulsation episode that is displayed for five consecutive time windows. The source of this pulsation candidate is 4U 1636–536, and starting time is 2006 Apr 23 11:21:38.8. *(top panel)* The light curve of the part of the observation that contains 336 s long candidate pulsation episode. The vertical dashed lines that have the same line style correspond to the starting and ending time of 256 s windows from which power spectra are calculated. *(bottom plots)* Z^2 power density spectra of the five sequential 256 s intervals indicated with vertical lines above. The signal at 579.66 Hz is clearly evident in all plots.

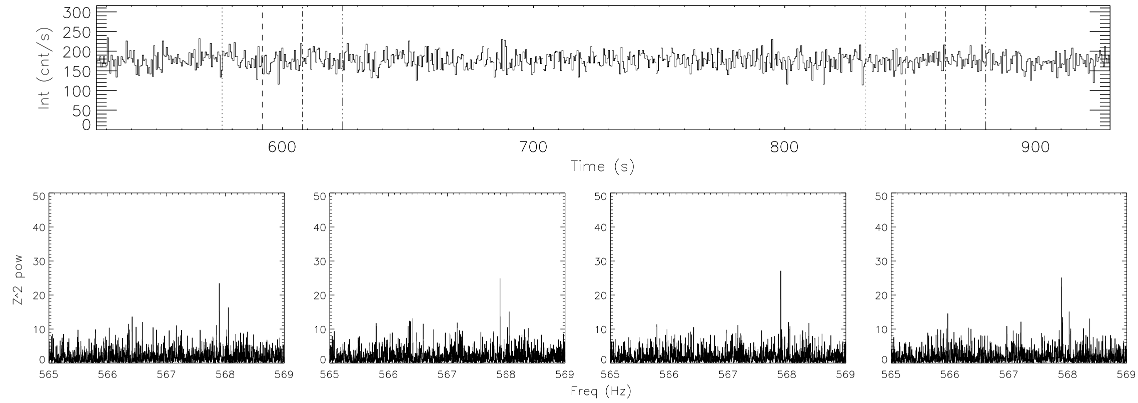

Figure 3.4 Example of a candidate pulsation episode that is displayed for four consecutive time windows. The source of this pulsation candidate is MXB 1658–298, and starting time is 2001 Aug 10 10:41:32.0. *(top panel)* The light curve of the part of the observation that contains 304 s long candidate pulsation episode. The vertical dashed lines that have the same line style correspond to the starting and ending time of 256 s windows from which power spectra are calculated. *(bottom plots)* Z^2 power density spectra of the four sequential 256 s intervals indicated with vertical lines above. The signal at 567.89 Hz is clearly evident in all plots.

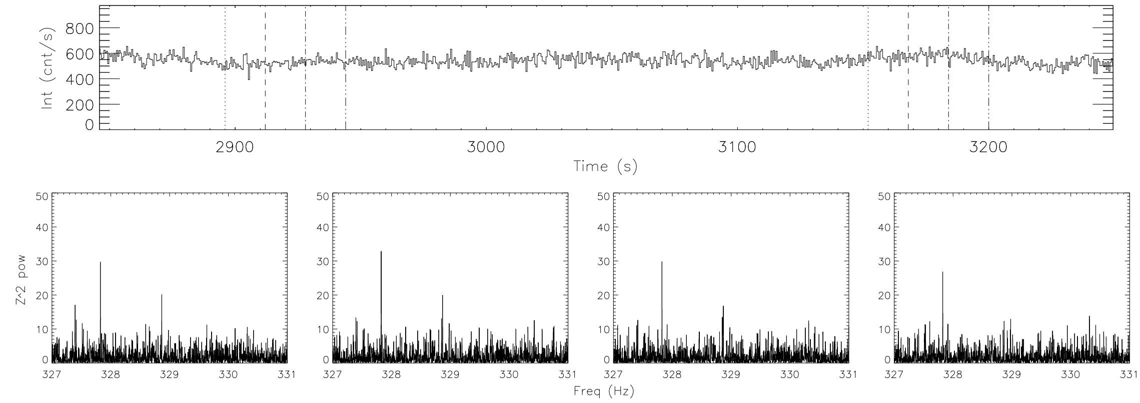

Figure 3.5 Example of a candidate pulsation episode that is displayed for four consecutive time windows. The source of this pulsation candidate is 4U 1702–429, and starting time is 2004 Apr 14 16:53:47.7. *(top panel)* The light curve of the part of the observation that contains 304 s long candidate pulsation episode. The vertical dashed lines that have the same line style correspond to the starting and ending time of 256 s windows from which power spectra are calculated. *(bottom plots)* Z^2 power density spectra of the four sequential 256 s intervals indicated with vertical lines above. The signal at 327.82 Hz is clearly evident in all plots.

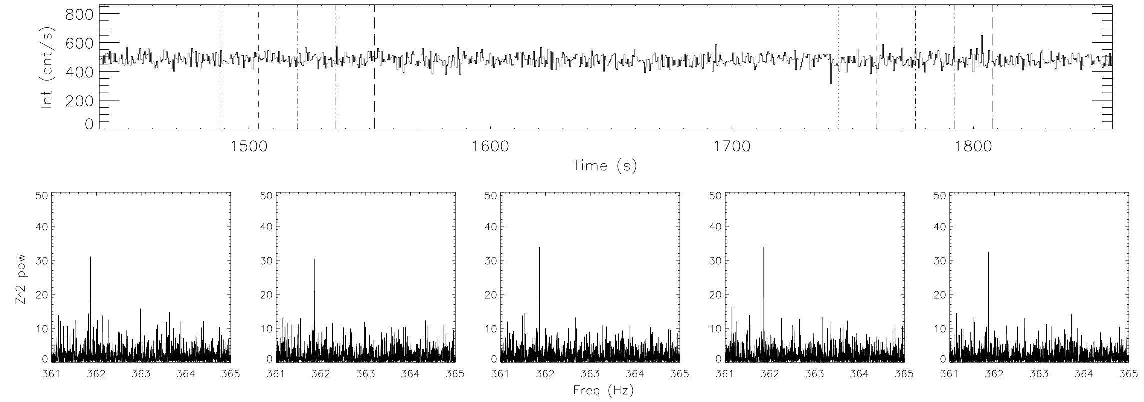

Figure 3.6 Example of a candidate pulsation episode that is displayed for five consecutive time windows. The source of this pulsation candidate is 4U 1728–34, and starting time is 2002 Mar 5 12:40:36.8. *(top panel)* The light curve of the part of the observation that contains 352 s long candidate pulsation episode. The vertical dashed lines that have the same line style correspond to the starting and ending time of 256 s windows from which power spectra are calculated. *(bottom plots)* Z^2 power density spectra of the five sequential 256 s intervals indicated with vertical lines above. The signal at 361.86 Hz is clearly evident in all plots.

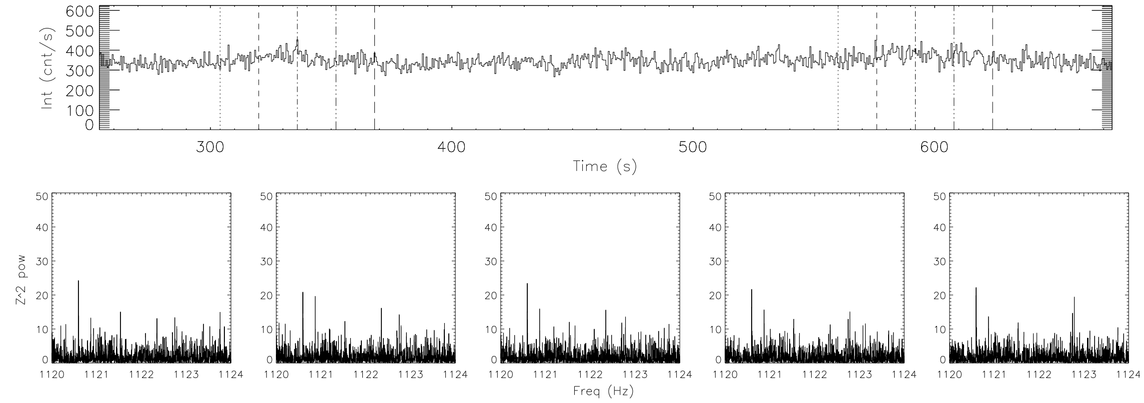

Figure 3.7 Example of a candidate pulsation episode that is displayed for five consecutive time windows. The source of this pulsation candidate is XTE 1739–285, and starting time is 2005 Nov 1 01:17:25.0. *(top panel)* The light curve of the part of the observation that contains 336 s long candidate pulsation episode. The vertical dashed lines that have the same line style correspond to the starting and ending time of 256 s windows from which power spectra are calculated. *(bottom plots)* Z^2 power density spectra of the five sequential 256 s intervals indicated with vertical lines above. The signal at 1120.59 Hz is clearly evident in all plots.

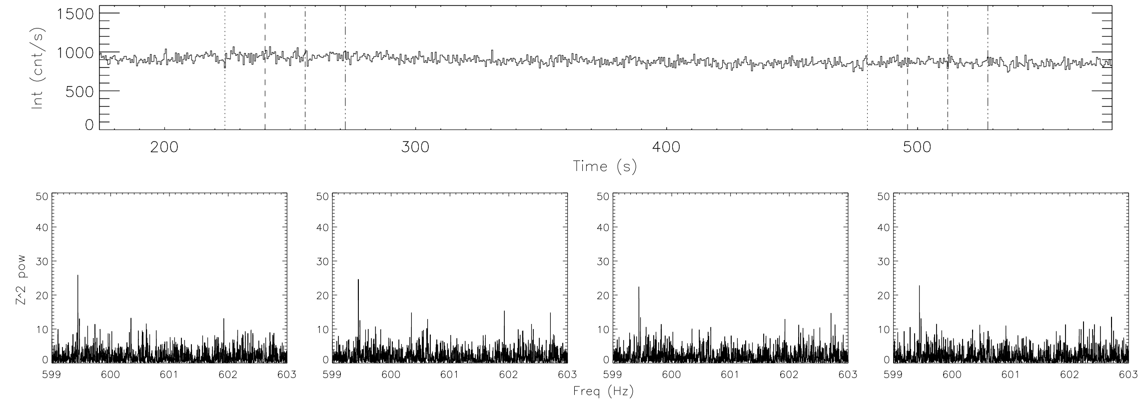

Figure 3.8 Example of a candidate pulsation episode that is displayed for four consecutive time windows. The source of this pulsation candidate is SAX J1750.8–2900, and starting time is 2008 May 12 07:21:28.9. *(top panel)* The light curve of the part of the observation that contains 320 s long candidate pulsation episode. The vertical dashed lines that have the same line style correspond to the starting and ending time of 256 s windows from which power spectra are calculated. *(bottom plots)* Z^2 power density spectra of the four sequential 256 s intervals indicated with vertical lines above. The signal at 599.44 Hz is clearly evident in all plots.

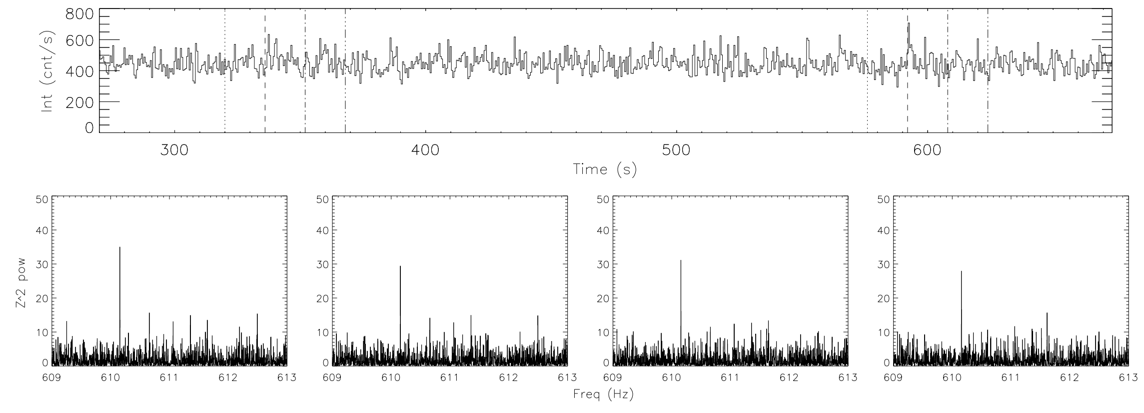

Figure 3.9 Example of a candidate pulsation episode that is displayed for four consecutive time windows. The source of this pulsation candidate is GS 1826–238, and starting time is 2006 Aug 15 16:48:43.0. *(top panel)* The light curve of the part of the observation that contains 304 s long candidate pulsation episode. The vertical dashed lines that have the same line style correspond to the starting and ending time of 256 s windows from which power spectra are calculated. *(bottom plots)* Z^2 power density spectra of the four sequential 256 s intervals indicated with vertical lines above. The signal at 610.16 Hz is clearly evident in all plots.

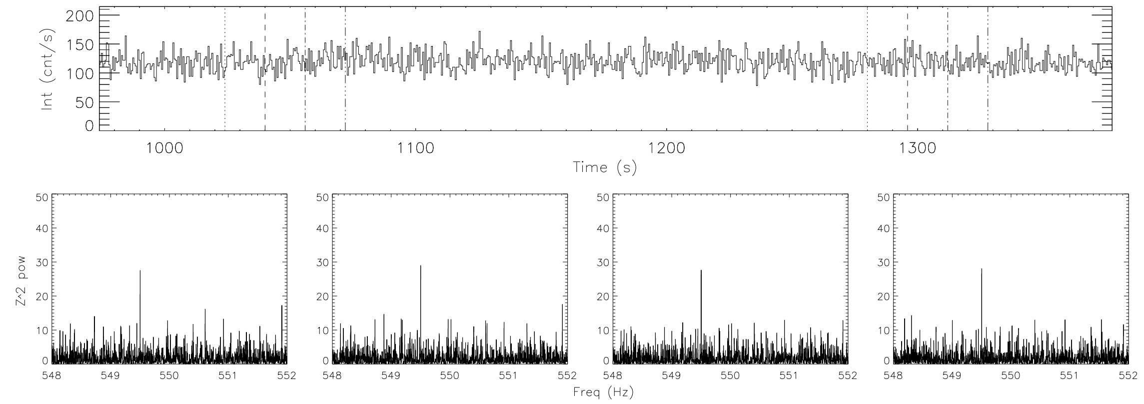

Figure 3.10 Example of a candidate pulsation episode that is displayed for four consecutive time windows. The source of this pulsation candidate is Aql X–1, and starting time is 2002 Mar 27 15:35:45.9. *(top panel)* The light curve of the part of the observation that contains 336 s long candidate pulsation episode. The vertical dashed lines that have the same line style correspond to the starting and ending time of 256 s windows from which power spectra are calculated. *(bottom plots)* Z^2 power density spectra of the four sequential 256 s intervals indicated with vertical lines above. The signal at 549.50 Hz is clearly evident in all plots.

Table 3.2 Results of the first tier pulsation search

Source	Time (UTC)[a]	t_{dur} (s)[b]	Leahy Power[c]	Z^2 Power[c]	f_L (Hz)[c]	sig_L (σ)[c]	Count Rate ($counts\ s^{-1}\ PCU^{-1}$)[d]
EXO 0748–676	**1998 Mar 14 01:02:04.9**	**320**	**35.9**	**35.7**	**44.51**	**3.94**	**36.8**
	1998 Jun 28 13:37:49.0	352	33.9	32.9	45.77	3.70	35.3
	2000 Mar 28 15:43:36.9	320	36.8	36.2	46.09	4.04	39.9
	2002 Sep 1 12:38:55.0	320	29.0	29.1	44.18	3.01	22.9
	2003 Feb 15 07:00:09.0	304	35.1	34.9	45.04	3.84	31.0
	2003 Aug 18 19:46:36.0	304	31.9	31.1	44.75	3.43	40.1
	2004 Apr 26 15:06:20.0	320	28.7	29.6	46.55	2.96	51.5
	2004 Apr 26 15:24:12.0	320	32.4	32.0	45.55	3.50	55.1
	2004 Nov 25 15:58:35.9	304	29.5	29.4	43.55	3.09	45.9
	2007 Feb 7 08:26:53.0	304	35.3	35.9	45.46	3.87	16.8
	2007 Aug 23 20:57:00.1	304	28.8	29.5	46.29	2.98	39.2
	2009 Jul 28 08:30:02.0	320	39.3	40.3	46.41	4.33	20.4
	1997 Jan 19 12:28:17.0	304	27.2	14.6	552.40	2.73	31.0
	2004 Sep 25 15:02:52.0	304	38.5	40.1	550.20	4.24	15.0
	2006 Sep 16 16:49:15.0	352	34.2	28.0	553.27	3.73	33.9
	2008 Feb 3 09:51:06.9	336	28.6	23.6	551.63	2.95	14.9
	2008 Feb 6 19:22:03.0	304	35.0	33.3	553.14	3.83	42.2
4U 1608–52	2002 Sep 1 09:25:30.0	304	32.0	28.6	620.13	3.45	746.3

Continued on next page

Table 3.2: continued from previous page

Source	Time (UTC)[a]	t_{dur} (s)[b]	Leahy Power[c]	Z^2 Power[c]	f_L (Hz)[c]	sig_L (σ)[c]	Count Rate ($counts\ s^{-1}\ PCU^{-1}$)[d]
	2002 Sep 28 18:26:26.0	320	31.7	29.7	620.53	3.40	46.2
	2003 Oct 4 17:11:39.0	304	30.6	20.6	620.80	3.25	70.8
	2007 Nov 1 06:39:10.1	**304**	**30.2**	**30.0**	**619.28**	**3.19**	**1298.8**
	2008 Nov 3 01:33:26.0	320	32.7	20.6	621.64	3.54	119.3
	2011 Dec 17 22:43:10.0	320	31.3	21.6	621.14	3.35	66.0
4U 1636–536	2001 Sep 30 14:10:38.0	336	35.3	31.1	580.08	3.86	242.2
	2001 Oct 3 17:41:54.0	304	29.2	26.6	582.29	3.04	246.8
	2002 Jan 8 14:31:39.2	320	30.4	22.4	579.86	3.21	201.7
	2002 Jan 8 18:13:14.4	336	35.8	39.5	580.41	3.93	186.1
	2002 Jan 14 08:40:11.7	304	28.8	30.2	582.35	2.98	158.9
	2002 Feb 28 18:30:51.8	320	27.7	23.2	582.29	2.81	534.1
	2002 Mar 19 17:09:15.9	304	29.3	20.1	579.61	3.05	387.5
	2005 Aug 29 18:49:32.2	320	35.3	27.8	580.05	3.87	112.3
	2005 Aug 30 11:57:00.2	320	32.0	22.5	580.11	3.44	119.1
	2006 Apr 23 11:21:38.8	**336**	**30.2**	**40.3**	**579.66**	**3.20**	**188.3**
	2006 Sep 12 07:42:51.0	304	28.1	26.2	580.12	2.87	99.3
	2007 Jun 20 03:08:59.2	320	33.7	35.3	582.26	3.67	246.4
	2007 Sep 28 21:15:40.4	320	33.5	18.6	580.06	3.64	184.0
	2008 Mar 15 17:32:12.9	336	30.2	31.5	580.66	3.19	273.4

Continued on next page

Table 3.2: continued from previous page

Source	Time (UTC)[a]	t_{dur} (s)[b]	Leahy Power[c]	Z^2 Power[c]	f_L (Hz)[c]	sig_L (σ)[c]	Count Rate ($counts\ s^{-1}\ PCU^{-1}$)[d]
	2008 Jul 3 19:28:59.0	304	27.2	25.4	581.33	2.73	225.8
	2008 Sep 11 03:57:02.1	304	30.6	24.7	581.77	3.25	145.7
	2008 Sep 25 01:50:51.0	304	27.1	18.7	580.67	2.71	434.3
	2009 Jan 17 04:31:21.9	304	31.1	22.1	579.60	3.31	127.7
	2009 Sep 10 07:56:26.0	336	31.1	30.1	580.55	3.31	126.5
MXB 1658–298	1999 Apr 29 17:43:55.9	304	28.6	21.6	566.32	2.95	95.3
	2001 Aug 10 10:41:32.0	**304**	**40.7**	**27.1**	**567.89**	**4.48**	**44.1**
4U 1702–429	2004 Jan 18 07:20:12.0	304	29.0	23.3	329.38	3.02	115.6
	2004 Apr 12 02:53:15.9	304	30.4	27.9	330.86	3.21	131.9
	2004 Apr 14 16:53:47.7	**304**	**32.4**	**32.8**	**327.82**	**3.49**	**181.1**
4U 1728–34	1997 Sep 24 12:59:09.1	336	28.8	28.5	364.31	2.99	477.3
	1999 Feb 28 02:41:15.9	304	31.7	31.2	363.27	3.40	212.7
	1999 Aug 19 18:22:52.0	320	33.3	31.0	361.54	3.61	622.3
	2000 Mar 7 17:06:24.8	320	30.8	27.7	363.05	3.28	274.2
	2001 Feb 2 19:33:54.9	304	32.0	31.4	363.78	3.45	176.4
	2001 Feb 8 22:24:59.7	320	35.1	30.0	361.64	3.84	135.7
	2001 Nov 15 12:45:25.0	320	32.6	29.2	362.89	3.53	152.6
	2002 Mar 5 12:40:36.8	**352**	**36.9**	**33.8**	**361.86**	**4.05**	**239.1**
	2006 Aug 1 16:43:07.0	304	29.6	23.8	363.99	3.10	317.1

Continued on next page

Table 3.2: continued from previous page

Source	Time (UTC)[a]	t_{dur} (s)[b]	Leahy Power[c]	Z^2 Power[c]	f_L (Hz)[c]	sig_L (σ)[c]	Count Rate ($counts\ s^{-1}\ PCU^{-1}$)[d]
	2007 Mar 16 02:26:34.9	320	30.5	24.2	362.37	3.23	357.3
	2007 Apr 16 20:43:46.9	352	32.8	28.8	361.11	3.55	378.5
XTE 1739–285	**2005 Nov 1 01:17:25.0**	**336**	**31.0**	**24.3**	**1120.59**	**3.30**	**116.5**
	2005 Nov 15 06:50:49.0	304	28.6	17.8	1123.96	2.95	85.5
SAX J1750.8–2900	**2008 May 12 07:21:28.9**	**320**	**31.3**	**24.6**	**599.44**	**3.35**	**445.9**
GS 1826–238	1998 Jun 23 19:45:00.9	352	34.9	21.5	609.09	3.81	99.2
	2004 Jul 20 20:13:02.0	304	30.3	15.9	611.85	3.21	142.7
	2006 Aug 10 05:10:35.1	304	31.9	29.2	612.91	3.43	120.4
	2006 Aug 15 16:48:43.0	**304**	**30.9**	**31.1**	**610.16**	**3.29**	**148.9**
Aql X–1	1997 Feb 27 07:10:21.9	304	31.4	20.6	549.83	3.36	204.8
	1997 Aug 28 15:46:53.0	320	39.3	31.9	548.24	4.33	439.5
	1998 Mar 10 22:48:18.9[e]	336	76.3	94.7	550.27	7.39	894.3
	2002 Mar 27 15:35:45.9	**336**	**33.0**	**27.6**	**549.50**	**3.57**	**29.9**
	2005 Apr 6 07:31:47.8	304	28.6	29.8	551.62	2.94	138.8
	2005 May 12 05:50:18.9	320	27.8	22.4	551.93	2.82	34.3
	2005 May 15 20:08:27.9	304	31.7	28.5	551.44	3.41	22.6
	2007 May 29 16:26:57.9	320	32.4	28.2	551.53	3.50	113.5
	2007 May 31 00:11:54.9	336	36.5	24.6	550.70	4.01	132.3
	2007 Jul 2 12:28:41.0	304	33.5	25.3	551.00	3.64	17.7

Continued on next page

Table 3.2: continued from previous page

Source	Time (UTC)[a]	t_{dur} (s)[b]	Leahy Power[c]	Z^2 Power[c]	f_L (Hz)[c]	sig_L (σ)[c]	Count Rate ($counts\ s^{-1}\ PCU^{-1}$)[d]

[a] Time (UTC) is the starting time of the candidate pulsation episode.

[b] t_{dur} is measured from the starting time of the first time segment to the ending time of the last time segment that fits our detection criterion of 2.5σ statistical significance in four consecutive time segments.

[c] Leahy power, Z^2 power, f_L and sig_L are obtained from the time segment where the strongest pulsation is observed within the corresponding pulsation episode.

[d] Count rates during the candidate pulsation episodes in the energy range of ∼3-27 keV.

[e] This is already reported as intermittent pulsations by Casella et al. (2008).

3.2 Binary Orbital Motion Corrected Search

Until this point, we searched for coherent pulsations in the data that only the barycentric correction was applied. However, binary orbital motion of the neutron star could smear out an already weak signal and make it undetectable. In our study, we used the appropriate relativistic orbit model (Blandford & Teukolsky, 1976) for the Doppler correction to be able to recover the smeared signal based on plausible orbital parameters. Formulation and the details of the time delay, t_d due to orbital motion can be found in Section 2.3.2.

In our search we assumed the orbit of the neutron star to be circular which is a plausible approximation for LMXBs ($e = 0$). This assumption reduced the number of free parameters to three that are the binary orbital period (P_b), projected semi-major axis (x) and the epoch of mean longitude equal to zero (T_0). Because of the lack of information and uncertainties about the epoch of mean longitude equal to zero, we decided to apply a $\pi/4$ radian sampling to the phase (ψ) of the circular orbit that corresponds to 8 trial phases in total.

This way, we aimed to test roughly all possible configurations that can effect the signal. For the six sources whose binary orbital periods were already reported (see Table 3.1), we limited the search interval of binary period to within 1 hr around their reported value, with a 0.1 hr sampling in those 2 hr intervals. For the rest of the sources whose binary period is unknown, we chose the range of the trial range of orbital periods to be 2–30.5 hr and applied 1.5 hr sampling to this time interval. Similar to the uncertainties about the epoch of mean longitude equal to zero (T_0) of the sources, projected semi-major axis (x) values of LMXB sources were also either unknown or highly uncertain. For this reason, we select a broad range of trial values from 0.01 to 1.91 light-s with 0.1 light-s sampling. Therefore, for each 256 s pulsation candidate time segment, the correction is applied for $8 \times 20 \times 20$ sets of parameters which span T_0, P_b and $a \sin i$ parameters, respectively.

We then searched for pulsations in the binary orbital motion corrected data by employing the Z^2 method between $f_s \pm$ 2 Hz as done before. By doing that, every correction that is applied with a different parameter set gave different statistical significance values for each time segment. Afterwards, we calculated the highest frequency shift that can occur (Δf_{max}) from the first order calculations (see eq. 4.4 in Section 4.2) and then located recovered pulsations by applying the following set of criterion: We require the recovered pulsations to have at least 3.5, 4.5 and 3.5σ statistical significance for three consecutive time segments and we require significance values for these three segments to be higher than before (that is, before the binary motion correction). We choose these significance levels since we wanted to put a significance criterion at least 1σ higher than the previous (2.5σ) for the detection of the recovered pulses. We require the improvement in the significance levels for three time segments to be achieved concurrently after corrected with the same parameter set. We also require the pulsations to be at the same frequency for these three time segments and the frequency of the recovered pulsation to be at most Δf_{max} away from the frequency of the pulsation before correction.

After applying this set of criterion we identified recovered pulsations for five sources; EXO 0748–676, 4U 1608–52, 4U 1636–536, Aql X–1, 4U 1728–34 out of 10 that showed pulsation candidates. We obtained degenerate pulsations for almost all time segments that show recovered pulsations. These pulsations were degenerate such that, for a single time segment there were many recovered pulsations obtained with different P_b, $a \sin i$, and ψ parameter sets. Moreover, pulsation strengths of recovered pulsations for a single time segment were at a similar level. The presence of degenerate recovered pulsations was expected because of the degenerate nature of Doppler effects. For example, to obtain similar Doppler effects for a trial orbital phase there should be a relation between P_b and $a \sin i$ such that if P_b is short, $a \sin i$ should also be shorter to compensate each other. For a more detailed discussion and simulations to understand the nature of this effect see Section 4.2.

Binary orbital period (P_b) of four of the five sources were already known (except 4U 1728–34). This helped us to eliminate the degenerate cases of recovered pulsations. We discarded the recovered pulsations that are obtained with a P_b that is different than the reported P_b. Furthermore, for each time segment we selected the parameter set that gives the the highest signal power among the ones that have the appropriate P_b. Binary period of 4U 1728–34 is unknown which resulted us to adopt a slightly different approach. Since sampling for the P_b parameter of 4U 1728–34 is 15 times larger than the ones that the binary periods are known, we decided to decrease the significance criterion of the detection of the recovered pulsation to 3.5, 4.0 and 3.5 from 3.5, 4.5 and 3.5. By doing so, we aimed to report more recovered pulsations and corresponding P_b, $a \sin i$ couples for such a highly unknown situation. We list the results of the recovered pulsations and the corresponding correction parameters in Table 3.3.

We also provide statistical significance values of the recovered pulsations as heat maps in Figures 3.11 to 3.15. In these figures, we present one recovered pulsation for each source listed in Table 3.3 to illustrate the degenerate nature of binary orbital correction. Each figure is made up of the statistical significance values of the

Table 3.3 Results of the binary motion corrected search

Source	Time (UTC)[a]	P_b (Hr)	$a \sin i$ (lt-s)	f_{Z^2} (Hz)	Z^2 Power	sig_{Z^2} (σ)
EXO 0748–676	1998 Mar 14 01:02:20.9	3.82	1.81	44.48	41.30	4.73
	2009 Jul 28 08:30:34.0	3.82	1.71	46.43	43.72	4.97
4U 1608–52	2007 Nov 1 06:39:58.1	12.89	1.91	619.28	39.42	4.54
4U 1636–536	2002 Jan 8 18:13:46.4	3.80	0.61	580.57	40.33	4.63
	2006 Apr 23 11:21:54.8	3.80	0.61	579.82	41.17	4.72
	2006 Apr 23 11:22:26.8	3.80	1.71	580.12	40.05	4.61
Aql X–1	1998 Mar 10 22:48:34.9	18.95	1.71	550.22	56.71	6.11
	1998 Mar 10 22:48:50.9	18.95	1.71	550.22	68.10	6.96
	1998 Mar 10 22:49:06.9	18.95	1.91	550.27	77.36	7.59
	1998 Mar 10 22:49:22.9	18.95	1.91	550.28	88.84	8.30
	1998 Mar 10 22:49:38.9	18.95	1.11	550.27	97.97	8.83
4U 1728–34[b]	1997 Sep 24 12:59:41.1	3.50	0.91	364.42	35.84	4.15
	1997 Sep 24 12:59:57.1	2.00	0.31	364.23	35.04	4.05
	1997 Sep 24 13:00:13.1	5.00	1.31	364.19	36.14	4.18
	1997 Sep 24 13:00:29.1	2.00	0.91	364.60	35.55	4.11
	1999 Feb 28 02:41:15.9	8.00	1.81	363.37	39.40	4.54
	2002 Mar 5 12:40:52.8	6.50	1.11	361.94	36.93	4.27
	2002 Mar 5 12:41:08.8	3.50	1.11	362.06	35.17	4.07
	2002 Mar 5 12:41:24.8	3.50	1.61	362.15	36.05	4.17

[a] Time (UTC) is the starting time of the 256 s time window.

[b] Detection criterion of recovered pulsations for 4U 1728–34 is different than other sources which is 3.5, 4.0 and 3.5 rather than 3.5, 4.5 and 3.5 for three consecutive time segments. See Section 3.2 for a more detailed discussion.

recovered pulsations obtained from a 256 second time segment. There are eight plots in each figure that correspond to eight orbital phase that we used while sampling the orbital phase parameter. Zeroth phase correspond to the mean longitude equal to zero which is measured from the ascending node (i.e. neutron star will be behind its companion at mean longitude of $\pi/2$ radian). Mean longitude of other seven phases can be calculated by multipyling the phase number with $\pi/4$ rad. Each plot in figures contains information of 20×20 statistical significance values that are obtained by applying the correction for a fixed orbital phase and 20×20 P_b, $a \sin i$ parameter sets. For visual purposes, colors of the intermediate parameter space between trial parameter sets are obtained by interpolation. In these figures, parameter sets that provide recovered pulsations meeting our detection criterion are indicated with an "o" symbol that is to say, they are the degenerate parameters sets. It can be inferred from the figures that the abundance of degenerate recovered pulsations obtained with different parameter sets makes it difficult to base conclusions about the orbital parameters of the source.

Note that we also report in Table 3.3 the binary motion corrected results for the intermittent 150 s pulsations in Aql X–1 (Casella et al., 2008). There were two different spin frequencies in literature that thought to be related with the spin frequency of EXO 0748–676 that are 45 and 552 Hz. We were able to obtain pulsation candidates at both of these frequencies in our first tier search. However, after applying and correcting the photon arrival times, we obtained recovered pulsations only around 45 Hz even though smearing effect of the Doppler modulation is increasing at higher frequencies.

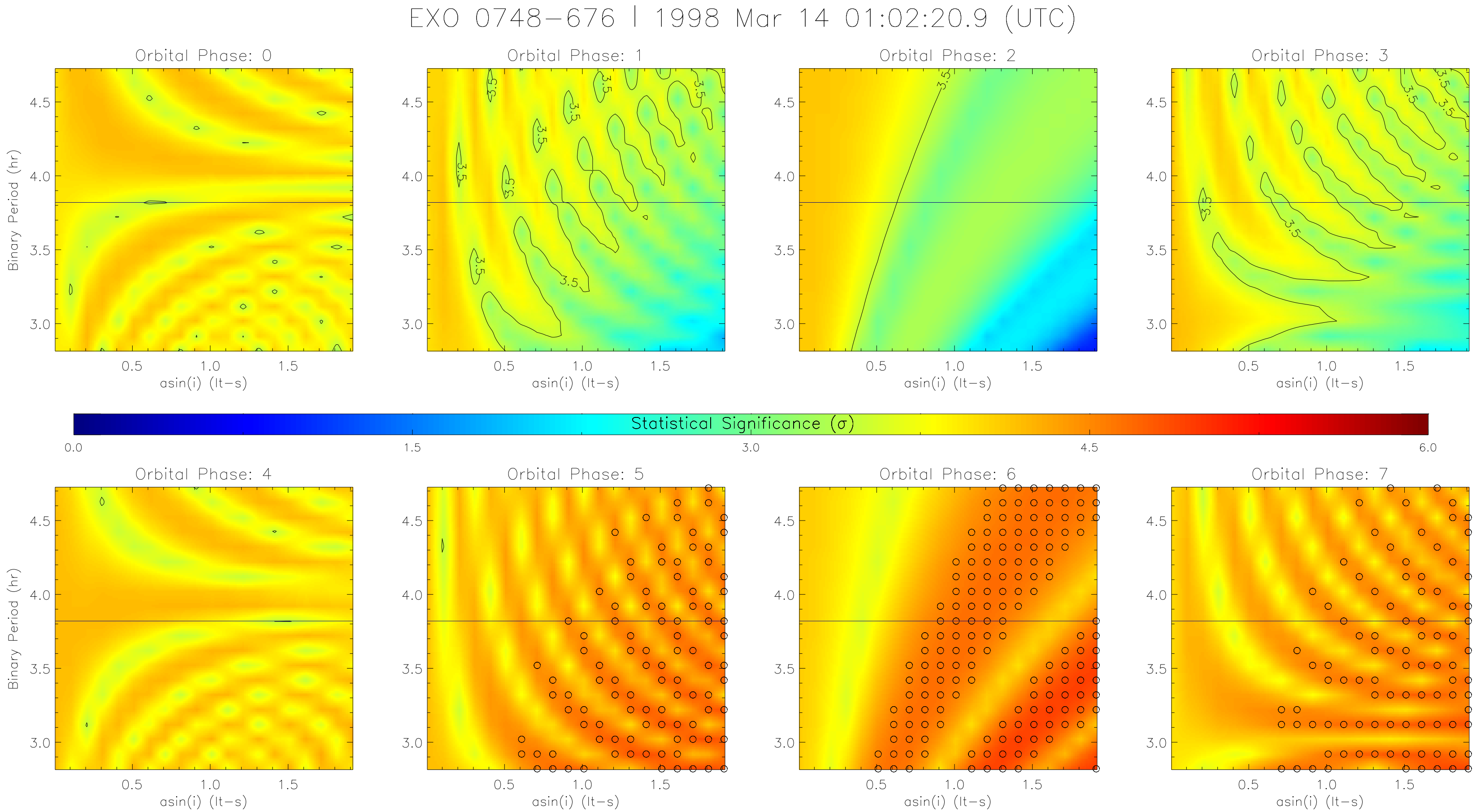

Figure 3.11 Heat map of the statistical significance values of the recovered pulsations that are obtained by applying the binary orbital motion correction to the 256 second time segment whose starting time is written in the title of the figure. Each plot corresponds to orbital corrections with different orbital phases. Colors in these plots correspond to the statistical significance values of the recovered signals obtained with different orbital phase, P_b and $a \sin i$ parameter sets. Solid horizontal line in the middle of each plot correspond to the reported binary period. Data points marked with "o" correspond to parameter sets that gives recovered pulsations meeting the detection criterion.

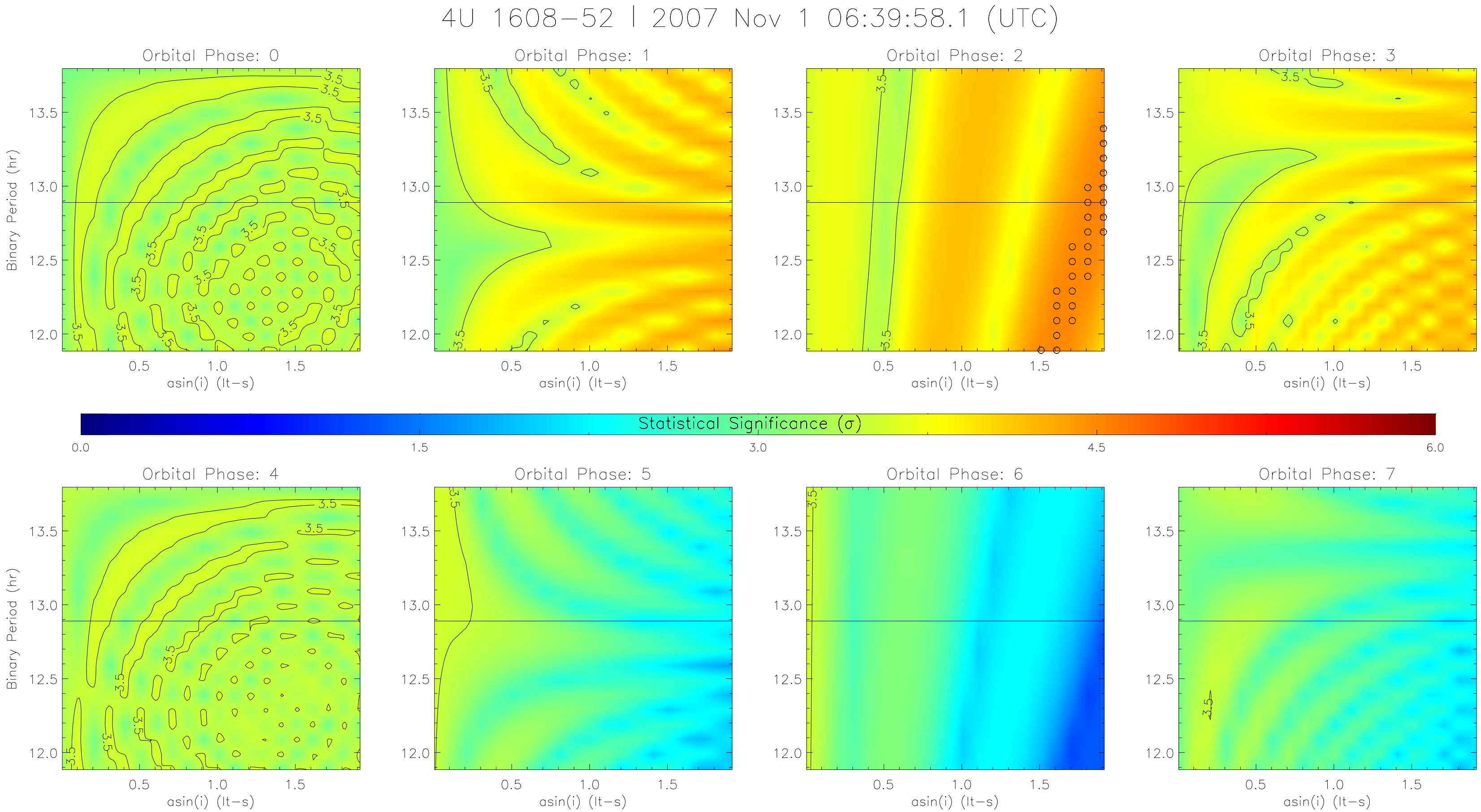

Figure 3.12 Heat map of the statistical significance values of the recovered pulsations that are obtained by applying the binary orbital motion correction to the 256 second time segment whose starting time is written in the title of the figure. Each plot corresponds to orbital corrections with different orbital phases. Colors in these plots correspond to the statistical significance values of the recovered signals obtained with different orbital phase, P_b and $a \sin i$ parameter sets. Solid horizontal line in the middle of each plot correspond to the reported binary period. Data points marked with "o" correspond to parameter sets that gives recovered pulsations meeting the detection criterion.

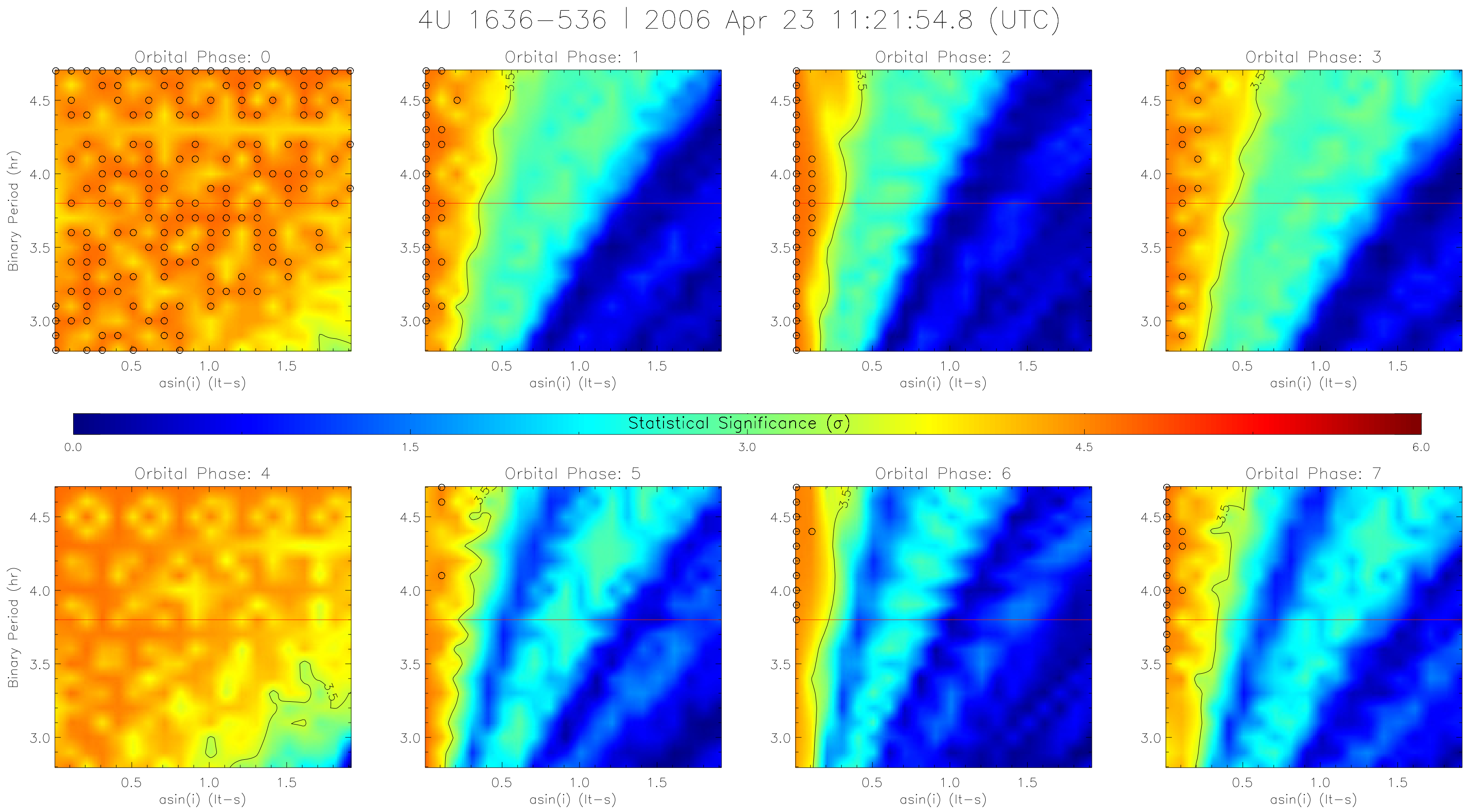

Figure 3.13 Heat map of the statistical significance values of the recovered pulsations that are obtained by applying the binary orbital motion correction to the 256 second time segment whose starting time is written in the title of the figure. Each plot corresponds to orbital corrections with different orbital phases. Colors in these plots correspond to the statistical significance values of the recovered signals obtained with different orbital phase, P_b and $a\sin i$ parameter sets. Solid horizontal line in the middle of each plot correspond to the reported binary period. Data points marked with "o" correspond to parameter sets that gives recovered pulsations meeting the detection criterion.

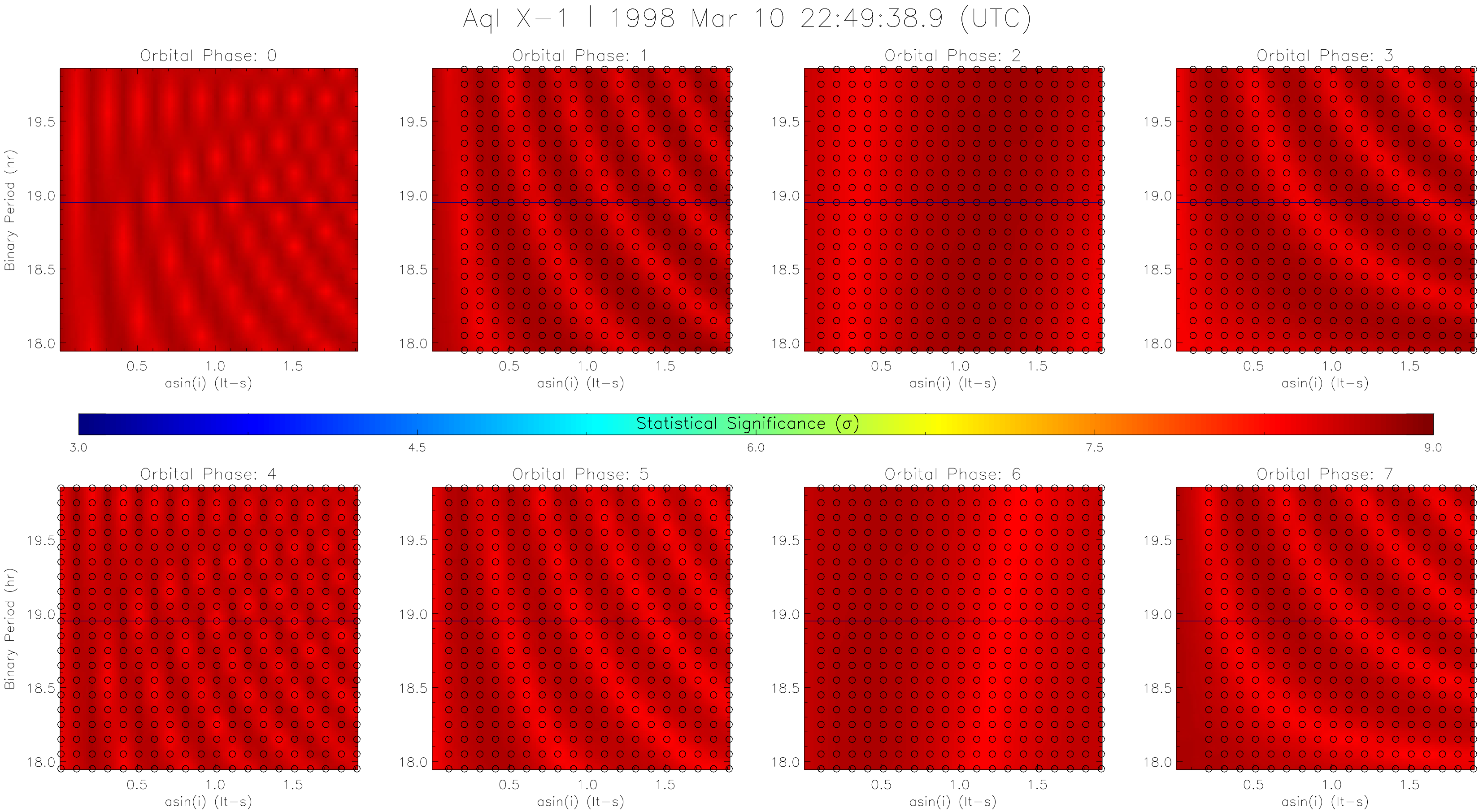

Figure 3.14 Heat map of the statistical significance values of the recovered pulsations that are obtained by applying the binary orbital motion correction to the 256 second time segment whose starting time is written in the title of the figure. Each plot corresponds to orbital corrections with different orbital phases. Colors in these plots correspond to the statistical significance values of the recovered signals obtained with different orbital phase, P_b and $a \sin i$ parameter sets. Solid horizontal line in the middle of each plot correspond to the reported binary period. Data points marked with "o" correspond to parameter sets that gives recovered pulsations meeting the detection criterion.

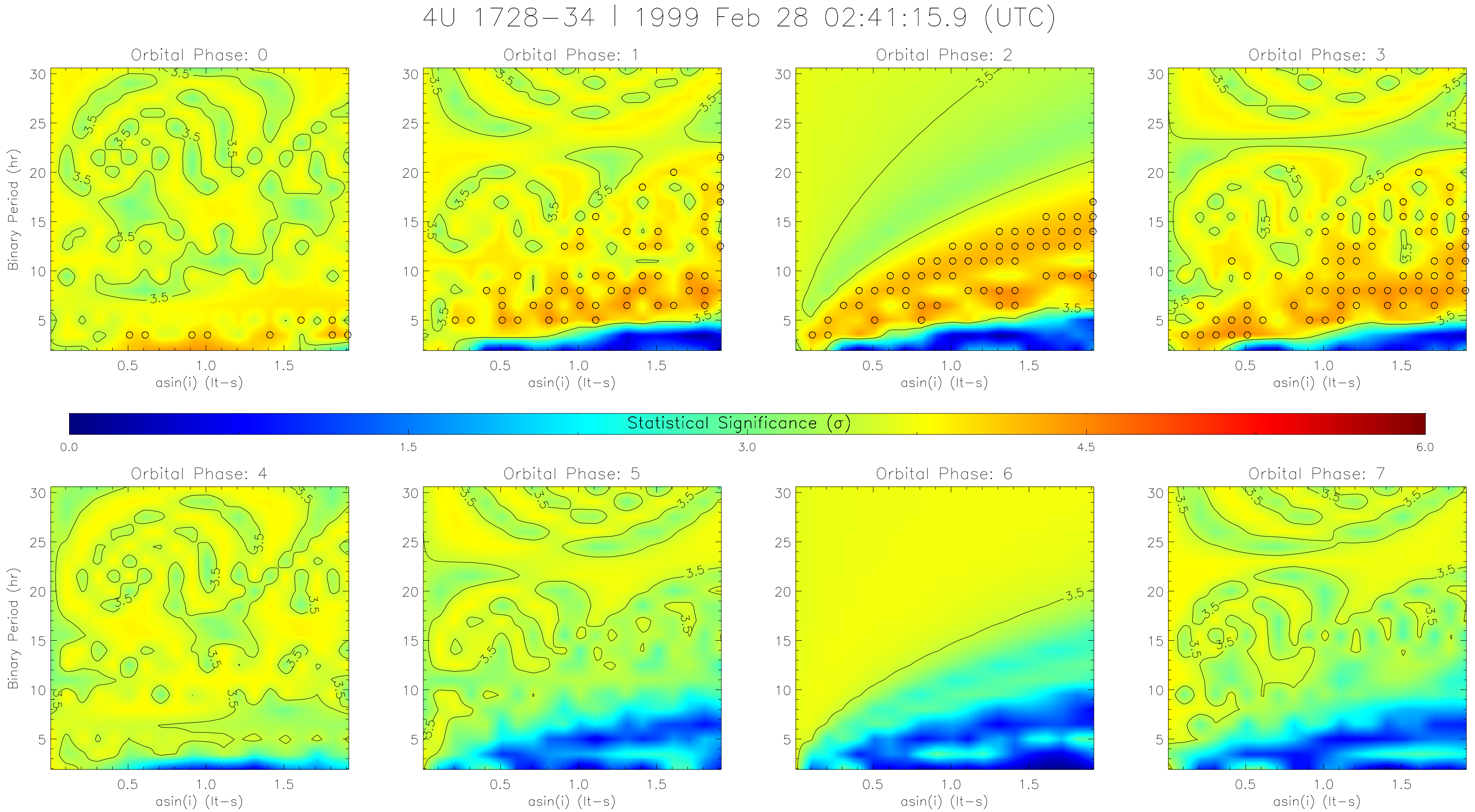

Figure 3.15 Heat map of the statistical significance values of the recovered pulsations that are obtained by applying the binary orbital motion correction to the 256 second time segment whose starting time is written in the title of the figure. Each plot corresponds to orbital corrections with different orbital phases. Colors in these plots correspond to the statistical significance values of the recovered signals obtained with different orbital phase, P_b and $a \sin i$ parameter sets. Data points marked with "o" correspond to parameter sets that gives recovered pulsations meeting the detection criterion. Note the different detection criterion (3.5,4.0,3.5σ) for 4U 1728–34 and the absence of the horizontal line because of the unknown P_b.

4. SIMULATIONS

We have also conducted two extensive simulations: one is to determine the limiting pulsed amplitude for detecting coherent signal in the persistent emission, and the other simulation is to better understand the effect of pulse smearing in the presence of binary orbital motion. We describe the setup of these simulations and present their results in this section.

4.1 Intensity Dependent Lower Bound on the Pulsed Fractional Amplitude

To obtain realistic lowest limits for pulsed fractional amplitudes, we added a pulsed emission component with a varying amplitude to the actual RXTE observations of the five investigated sources: 4U 1608–52, 4U 1636–53, Aql X–1, EXO 0748–676 and 4U 1728–34. These sources were selected in order to cover a wide regime of X-ray intensities. We only used observations with all 5 PCUs operational, and considered the first 256 s of data segment after the times of thermonuclear bursts were eliminated.

For the pulsed emission, we have chosen a template pulse frequency of 500 Hz. It is not only a plausible value for the spin frequency of neutron star in LMXBs and also far enough from burst oscillation frequencies of the selected five sources so that no bias would be included in our resulting light curves. For each 256 s time segment, we first generated pulsed light curves by using the Poisson process that has an oscillating mean,

$$\mu_p = A \sin 2\pi f_p t + A \tag{4.1}$$

where f_p is the pulsation frequency and A is the amplitude of the pulse. We selected bin size of the light curves to be 1/2048 s to be consistent with our pulse search. Then this synthetic light curve is randomly converted to photon arrival times by uniformly distributing the number of photons in each bin into the corresponding time interval. Synthetic photon arrival times are then appended to the real 256 s long data. The resulting light curve was then used for FFT analysis. Finally, the statistical significance of the Leahy power in the 500 Hz frequency bin was calculated with the same approach before. This process is repeated for 150 fractional amplitude values that are ranging from 0.00008 to 0.12 by varying the amplitude (A) of the synthetic light curve. Among these trials, lowest fractional amplitude value that succeed to provide a pulsation with a minimum statistical significance of the 3σ was recorded for each observation. We present the resulting limiting pulsed amplitudes as a function of intensity in Figure 4.1. Besides the simulation, we also analytically obtained fractional amplitude as a function of intensity in the case a non-randomized perfect sinusoidal was added to the real data. The relation we obtained can be formulated as

$$A_{frac} = \sqrt{\frac{2P_{3\sigma}}{t_{wind} I}} \propto I^{-0.5} C \tag{4.2}$$

where $P_{3\sigma}$ is the Leahy power corresponding to 3σ statistical significance (according to the choice of N_{trials}), t_{wind} is the window size and I is the intensity. It can be seen from the formula that fractional amplitude (A_{frac}) is inversely proportional with the square root of I multiplied with a constant (C). The constant may vary according to the choice of t_{wind} and N_{trials} parameters however, relation between A_{frac} and I is invariant. With our choice for t_{wind} and N_{trials} we found C to be 0.515 and it can be seen that the best fitting line ($y = 0.515x^{-0.492}$) in Figure 4.1 is in agreement with the analytical solution obtained by adding a pure sinusoidal on real data.

Results of our simulation suggest that the pulsed fractional amplitude should be higher for observations with lower intensities for the pulsation signal to be statistically considered as a detection. Therefore, pulsed fraction 3σ lower limits for fainter sources such as EXO 0748–676 is higher compared to the lower limits of brighter sources such as Aql X–1. To put it in another way, in the high intensity regime pulsed fraction lower detectability limits drop down to 0.006 whereas the pulsed fraction lower detectability limits goes up to 0.08 in the low intensity regime. It can be also seen from the Figure 4.1 that the solid line is dividing the parameter space into two. The upper region above the line corresponds to the detection region with

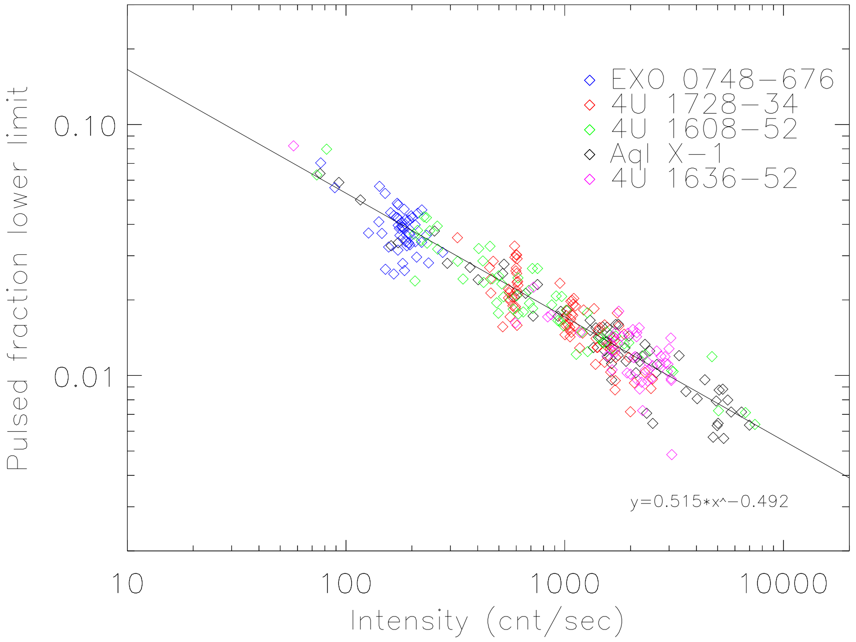

Figure 4.1 The 3σ detection limit of pulse fractions obtained from 303 RXTE observations of the five color-indicated sources. The solid line represents the best fit to all detection limits.

statistical significance $> 3\sigma$ and the lower region corresponds to the no detection region where statistical significance of the pulsation is $< 3\sigma$. Overall, this simulation provide a general picture of the trade-off between the commonly used pulsed fractional amplitude and intensity parameters for pulse detection.

4.2 Effects of Binary Motion on the Pulsed Signal

We have performed this set of simulations to exhibit the extend of smearing of the pulsed signal due to binary orbital motion of the neutron star. First, we generated a 256 s long light curve with 1/2048 s time resolution by sampling from a Poisson distribution that has an oscillating mean where the oscillation frequency is the frequency of the pulsed signal. The mean of the Poisson process is set to

$$\mu_p = A \sin 2\pi f_p t + B \tag{4.3}$$

where f_p is the spin frequency of the neutron star, A is the amplitude of the randomized pulsation and B is the amplitude of the Poisson distributed background. We set B to be 0.125, corresponding to an average count rate of 256 counts/s that is a plausible level for the PCA. We performed simulations for two spin frequency values; 300 Hz and 600 Hz which mark typical lower and upper bounds for burst oscillations in LMXBs. We randomly generated photon arrival times for each light curve using a uniform distribution. We set ten levels for the significance of the pulse: 3.83, 4.0, 4.37, 4.5, 4.88, 5.0, 5.38, 5.0, 5.89, 6.0σ. We again considered a circular orbit ($e = 0$), assume a neutron star mass of 1.4 $M_{\odot}$ and the donor star mass of 0.5 $M_{\odot}$. After generating the synthetic photon arrival times, we smeared the signal by applying the prescription of Blandford & Teukolsky (1976) for P_b values between 0.01 hr and 20 hr in 200 steps. The semi-major axis of the binary could be calculated using Kepler's 3^{rd} law for the binary period used and a given inclination angle (i). Besides binary period and inclination angle there is one more free parameter which is binary phase (ψ). Our simulation grid included six values of inclination angle from 15° to 90° with 15° steps, and again eight phase steps from 0 to $7\pi/4$ rad. We calculate the maximum frequency shift that can happen due to the Doppler effect

$$\Delta f_{max} = f_p \left| \frac{P_b}{P_b - 2\pi a \sin i} - 1 \right| \tag{4.4}$$

where $a \sin i$ is the projected semi-major axis. We then determined the maximum power between $f_p \pm \Delta f_{max}$ for each smeared signal. For each inclination angle and phase, maximum power of the smeared spectrum becomes a function of binary period where short binary period corresponds greater smearing and long binary period corresponds to less smearing. We fit binary period vs. maximum power trends with a function;

$$f_{mp}(P_b) = \begin{cases} C_0 - C_1 e^{-C_2 C_3} & \text{if } P_b \leq C_3 \\ C_0 - C_1 e^{-C_2 P_b} & \text{if } P_b > C_3 \end{cases} \tag{4.5}$$

where C_n are the fitting parameters with which we can determine the binary period lower bounds that the signal power drops under the 3σ statistical significance level. In other words, the pulse would be smeared and would not be detected at the 3σ significance if the binary period is shorter than the threshold period value. Here, we were interested only in phases where the maximum and minimum smearing take place. Finally, we took the weighted average of the lower bounds of signals with different significance at the same frequency, inclination and phase.

The upper lines in Figure 4.2 are the maximum smearing phase lower bounds and the lower lines are the minimum smearing phase lower bounds for the detection (3σ) of the signal in the presence of the Doppler effect. It can be seen from the figure that the maximum and minimum smearing phase lower bounds are dividing the parameter space into three regions. Upper region is the part of the parameter space where we expect to see low smearing since even in the highest smearing phase, we do not observe the signal strength to drop below 3σ significance level. Middle region is the part where intermediate level of smearing is expected. In this region, the signal is buried within the noise by the Doppler effect in the maximum smearing phase of the orbit. However, it is still detectable in the minimum smearing phase. Lastly, lower region is the part where we expect to observe high level of smearing. Therefore, the signal would be buried well under the noise level even in the lowest smearing phase.

Lower detection bounds for signals with pulsation frequencies of 300 Hz and 600 Hz are different since the Doppler effect have dependence on frequency. Just as we expect to observe in Doppler effects, the signals with higher frequency are affected more from the smearing for the same binary period and inclination. That is the reason for us observing lower bounds of 600 Hz signal to be relatively higher than the lower bounds of 300 Hz signal.

These results can be used to envision the results of computationally expansive Doppler searches. For example, a signal of 300 Hz from a system with an inclination of 45°, the Doppler restoration would be feasible if the binary orbital period is shorter than 4 hours. Furthermore, binary orbital periods shorter than about 1.8 hours would put this system in the high smearing regime, therefore, it would be an appealing candidate for the Doppler search. Similarly, if a system with an average inclination (45°) shows a signal at 600 Hz, it will be a feasible candidate to recover any buried signal via Doppler search if the binary orbital period is less than about 7.3 hours. Any intermediate cases can be inferred by using these two figures.

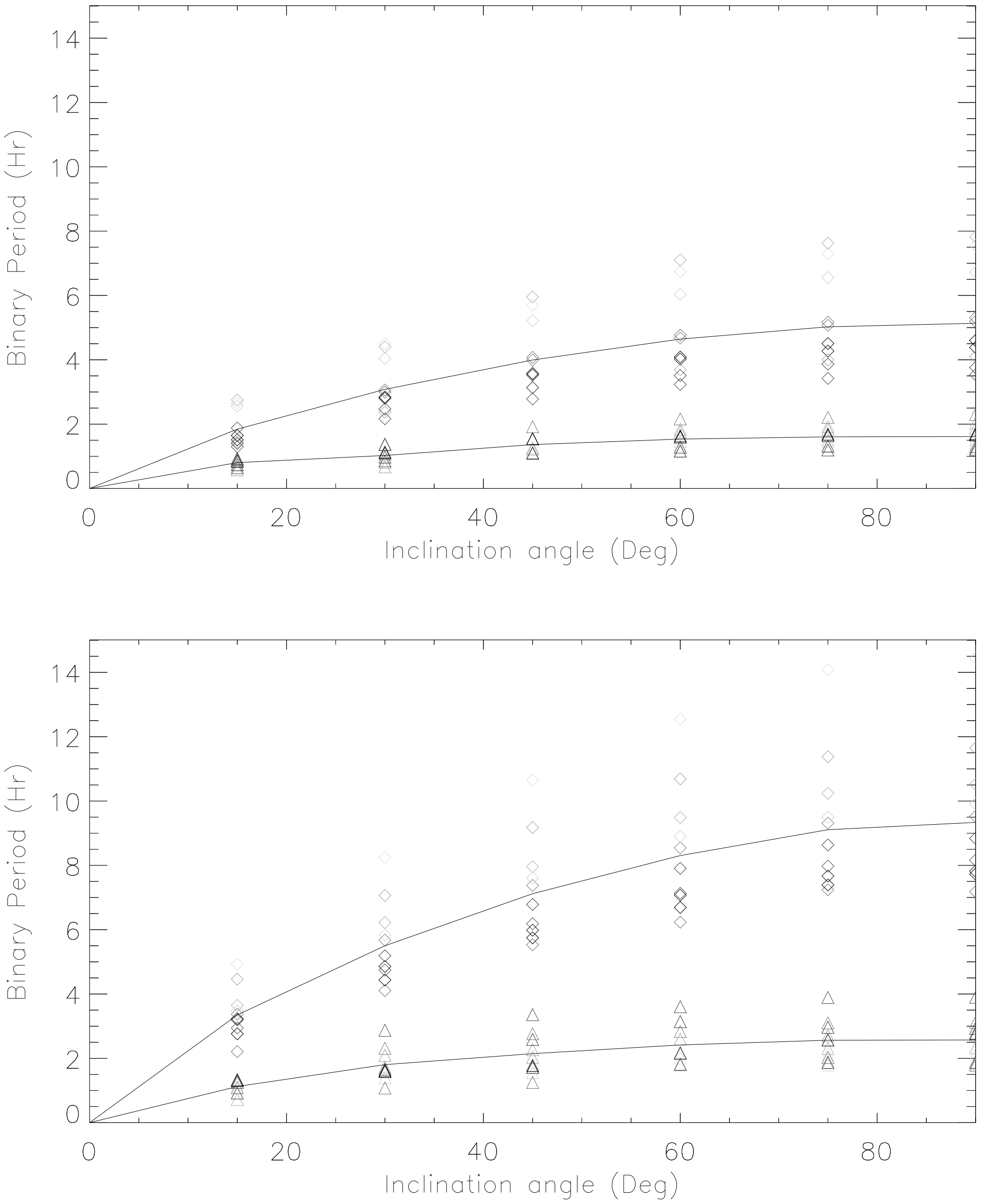

Figure 4.2 Detection boundaries of 300 Hz *(top plot)* and 600 Hz *(bottom plot)* pulsations that were subject to the orbital smearing. Diamonds and triangles are the (3σ) detection limits of binary period parameter at the highest and lowest smearing phases for a given inclination angle. Darkness of the diamonds correspond to the initial statistical significance of the smeared pulses that are ranging from 4.0 to 6.0σ. Solid lines are the weighted averages of the 3σ detection lower bounds of the binary period parameter for minimum and maximum smearing phases. Three region that the solid lines divide the parameter space into are low, intermediate and high smearing regions from top to bottom.

5. DISCUSSION AND CONCLUSIONS

We have performed one of the most comprehensive search for intermittent pulsation episodes in non-pulsing LMXBs. In particular, we have accounted for the binary orbital motion systematically in our extensive investigations. Recently, Messenger & Patruno (2015) and Patruno et al. (2018) also accounted for the Doppler shift in searching pulsations from LMXBs with their semi-coherent search. Their work differ from ours at a fundamental level: They aimed to detect continuous but weak pulsations, contrary to our search for intermittent pulsation episodes. Furthermore, eight out of 12 of the LMXB sample in semi-coherent search did not show burst oscillations. This made their parameter space significantly wider for these LMXBs contrary to more confined spin frequency parameter in our work thanks to the previously reported burst oscillations for the LMXBs. Note that we have nine different LMXBs in addition to four common with their work, namely; Aql X–1, 4U 1636–536, 4U 1608–52 and XTE 1739–285.

Detection of a single ∼150 s long pulsation episode (Casella et al., 2008) in the entire archival RXTE data of Aql X–1's persistent emission phase clearly show that the intermittent pulsations can be very rare (0.009% of the total 1645 ks observed time). Note that the pulsation episodes in other sources are also rare with respect to the total observation time: 0.023% for EXO 0748–676, 0.012% for 4U 1608–52, 0.016% for 4U 1636–536 and 0.062% for 4U 1728–34. We should note here that occurrence rate for 4U 1728–34 is expected to be higher since we lowered significance criterion for this source (See Section 3.2). Besides these recovered pulsations, we also found pulsation candidate episodes that contain weak pulsations around the burst oscillation frequencies for all 13 LMXBs in our sample. These candidate episodes are also short and rare compared to the total searched time of each source: 0.24% for EXO 0748–676, 0.08% for 4U 1608–52, 0.13% for 4U 1636–536, 1.84% for MXB 1658–298, 0.07% for 4U 1702–429, 0.21% for 4U 1728–34, 0.52% for XTE 1739–285, 0.15% for SAX J1750.8–2900, 0.12% for GS 1826–238, and 0.19% for Aql X–1

Strohmayer et al. (2018) employed the same binary orbital motion correction to account for Doppler smearing in an accreting millisecond X-ray pulsar system, IGR

J1762–6143 with an ultra-compact orbit (binary orbital period is ∼38 min). They found that the orbital delays weaken the pulsation such that after the correction to its NICER data, Z^2 power of the pulsation increase up to ∼196 which is almost 4 times the previous value (∼55). However, their work differs from ours on a fundamental aspect. IGR J1762–6143 shows strong pulsations as side bands even when no correction was applied. Correcting the photons put the side band structure together and result with a stronger centered pulse. In our approach, we do not observe clear pulsations as side band structures in the non-corrected data since the strength of the pulsations that we have been looking for were not strong enough to be detected after smearing. Nevertheless, it is important to remark that side band structured pulses of IGR J1762–6143 together with our simulations (See 4.2) clearly show that smearing effect of the binary orbital motion plays a key role in disappearance of already weak pulsations. This makes it almost mandatory to apply the Doppler correction to the photon arrival times before searching weak pulsations especially for compact (short P_b) sources considering the high uncertainties in the inclination angles.

We were able to determine orbital inclination of four systems, based upon our criterion that the search in the Doppler corrected data would yield the strongest signal. We suggest the projected semi-major axis ($a \sin i$) value of about (5.1–5.4)$\times 10^8$ m for EXO 0748–676, and 5.7×10^8 m for 4U 1608–52. For typical orbital separations (a) that can be calculated from the known binary periods, the orbital inclination of these two systems turned out as 29.0–30.9 and 13.9 degrees, respectively. Our search for projected semi-major axis of 4U 1636–536 and Aql X–1 concentrate around two values: 1.8×10^8 or 5.1×10^8 m for the former, and 3.3×10^8 or (5.1–5.7)$\times 10^8$ for the latter. These correspond to 9.9 or 29.1 degrees of inclination for 4U 1636–536 and 6.2 or 9.6–10.7 degrees for Aql X–1. We would like to note that, donor mass and neutron star mass are assumed to be 0.5 and 1.4 $M_\odot$ respectively for calculating the orbital separations. Highly degenerate recovered pulsations and their scattered orbital parameters in the $P_b - a \sin i$ plane made it impossible to determine orbital parameter estimates for 4U 1728–34. Two recovered episodes of pulses for EXO 0748–676 were found at the frequencies of 44.5 and 46.4 Hz. We found pulsation candidate episodes around 552 Hz, which is the other suggested frequency, and also there are other studies supporting that (Balman, 2009; Jain & Paul, 2011). However, we did not detect any recovered pulsations after the Doppler correction around the higher frequency. In the light of these results, we argue that the 45 Hz may be the actual spin frequency of EXO 0748–676 rather than 552 Hz.

We have also investigated whether X-ray intensity (that is a measure of mass accretion rate) is different during those pulsation episodes. We compare the average count rate for each source (listed in Table 3.1) to the source rates during the episodes of coherent pulsations (listed in Table 3.2). We find no systematic trend in X-ray intensities, neither higher nor lower than their long term averaged values. We, therefore, suggest that the appearance of pulsations are not linked to any sudden change in the accretion rate.

The lack of pulsations in these bright LMXB sources may not be solely related to the Doppler effects. There are already numerous suggestions attempting to explain the reason of intermittent pulsations. Sporadic behaviour and uncommon nature of such periodicities force the explanations to be somehow related with a rare incident or asymmetry that might be taking place close to the neutron star surface. These explanations can be roughly divided into two categories: one group of explanations assume that the pulsation is temporary while other group assume that the pulsation is always present however so weak that we cannot detect it.

One possible explanation for the lack of pulsations that belongs to the first group is the scattering of the beamed emission by the optically thick media. However, this approach was challenged by Göğüș et al. (2007) where they argued through spectral investigations that the optical depth τ of the surrounding corona is not thick enough to smear out the pulsations. In order for this explanation to work, temperatures of scattering electrons should be very low ($\lesssim$ 10 keV) so that the optical depth would be large enough to screen. The pulsations would then become visible only during a spectral variability, in presence of a local hole in the screening medium or in presence of other unique asymmetric geometries (Casella et al., 2008). In such a scenario, one would also expect a dependence of the presence of the pulsation on the accretion rate as in such systems the coronal properties are strong function of the accretion rate. Such a correlation was found to absent in our analysis.

The second group of explanations is generally related to the magnetic channeling. Neutron stars in LMXBs are weakly magnetized. Therefore, they are typically unable to stop and focus the incoming matter. The appearance of pulsations could either be due to a sudden change in the amount of channeled matter or the strength of their magnetic field could suddenly increase (at least locally) and become capable of channeling matter. The second scenario might occur if there is a sudden decrease in the Ohmic diffusion time which could happen due to a starquake, local disruption of screening currents or magnetic reconnections (Casella et al., 2008). It is essential to study multipolar magnetic fields in such neutron stars to find an evidence for strengthening the magnetic fields. Recent serious efforts to understand magnetic field structure of neutron stars by ray-tracing technique (Bilous et al., 2019) may provide new insights on this front.

Another explanation in the second group argues that the nearly aligned magnetic and spin axes may be the reason of the lack of pulsations (Lamb et al., 2009a,b). They simulated hot spots that have a radii of 25° on a neutron star that has a mass of 1.4 $M_{\odot}$, a radius of 10 km and a spin frequency of 400 Hz. With those simulations they measured the fractional rms amplitudes that are obtained with various observer inclinations and spot inclinations. Messenger (2011) argued that this scenario cannot explain the 150 s intermittent pulsation episode seen from Aql X–1 since such a strong pulsation can only be observed with a sudden and dramatic shift ($\sim 15°$) of the hot spot which should be locked to the magnetic axis for a long time. Pulsations that we identified in our search are not as strong as the intermittent pulsations seen from Aql X–1 and the observer inclinations are highly uncertain for the sources searched. These facts, therefore, make it difficult to attribute this model with our pulse detections.

Another alternative within the second group explanations is nuclear burning. We expect nuclear powered oscillations to last typically a few seconds. However, Strohmayer & Markwardt (2002) reported a long-lasting pulsation during a superburst of 4U 1636–536. This indicates that coherent and longer lasting oscillations may also be related with nuclear burning. This explanation cannot be related with our results since we carefully identified the bursts and eliminated their times from our searched sample. There could, in principle, be nuclear burning events which might not be seen radiatively (as thermonuclear bursts) but the stored energy could instead give rise to intermittent coherent oscillations.

BIBLIOGRAPHY

Alpar, M. A., Cheng, A. F., Ruderman, M. A., & Shaham, J. 1982, Nature, 300, 728, doi: 10.1038/300728a0

Altamirano, D., Casella, P., Patruno, A., Wijnands, R., & van der Klis, M. 2008, ApJL, 674, L45, doi: 10.1086/528983

Altamirano, D., Linares, M., Patruno, A., et al. 2010, MNRAS, 401, 223, doi: 10.1111/j.1365-2966.2009.15627.x

Andersen, B. C., & Ransom, S. M. 2018, ApJL, 863, L13, doi: 10.3847/2041-8213/aad59f

Anderson, S. B., Gorham, P. W., Kulkarni, S. R., Prince, T. A., & Wolszczan, A. 1990, Nature, 346, 42, doi: 10.1038/346042a0

Balman, S. 2009, The Astronomer's Telegram, 2097, 1

Bhattacharyya, S. 2009, Current Science, 97, 804

Bhattacharyya, S., Strohmayer, T. E., Markwardt, C. B., & Swank, J. H. 2006, ApJL, 639, L31, doi: 10.1086/501438

Bhattacharyya, S., Thampan, A. V., Misra, R., & Datta, B. 2000, ApJ, 542, 473, doi: 10.1086/309502

Bildsten, L. 2000, in American Institute of Physics Conference Series, Vol. 522, American Institute of Physics Conference Series, ed. S. S. Holt & W. W. Zhang, 359–369

Bilous, A. V., Watts, A. L., Harding, A. K., et al. 2019, ApJL, 887, L23, doi: 10.3847/2041-8213/ab53e7

Blandford, R., & Teukolsky, S. A. 1976, ApJ, 205, 580, doi: 10.1086/154315

Brainerd, J., & Lamb, F. K. 1987, ApJL, 317, L33, doi: 10.1086/184908

Buccheri, R., Bennett, K., Bignami, G. F., et al. 1983, A&A, 128, 245

Casella, P., Altamirano, D., Patruno, A., Wijnands, R., & van der Klis, M. 2008, ApJL, 674, L41, doi: 10.1086/528982

Chadwick, J. 1932, Proceedings of the Royal Society of London Series A, 136, 692, doi: 10.1098/rspa.1932.0112

Chevalier, C., & Ilovaisky, S. A. 1991, A&A, 251, L11

Done, C., Gierliński, M., & Kubota, A. 2007, A&ARv, 15, 1, doi: 10.1007/s00159-007-0006-1

Frank, J., King, A., & Raine, D. J. 2002, Accretion Power in Astrophysics: Third Edition

Galloway, D. K., Lin, J., Chakrabarty, D., & Hartman, J. M. 2010, ApJL, 711, L148, doi: 10.1088/2041-8205/711/2/L148

Galloway, D. K., Muno, M. P., Hartman, J. M., Psaltis, D., & Chakrabarty, D. 2008, ApJS, 179, 360, doi: 10.1086/592044

Ghosh, P., & Lamb, F. K. 1979, ApJ, 232, 259, doi: 10.1086/157285

Göğüş, E., Alpar, M. A., & Gilfanov, M. 2007, ApJ, 659, 580, doi: 10.1086/512028

Harding, A. K. 2013, Frontiers of Physics, 8, 679, doi: 10.1007/s11467-013-0285-0

Hartman, J. M., Chakrabarty, D., Galloway, D. K., et al. 2003, in AAS/High Energy Astrophysics Division #7, AAS/High Energy Astrophysics Division, 17.38

Hewish, A., Bell, S. J., Pilkington, J. D. H., Scott, P. F., & Collins, R. A. 1968, Nature, 217, 709, doi: 10.1038/217709a0

Hynes, R. I. 2010, arXiv e-prints, arXiv:1010.5770. https://arxiv.org/abs/1010.5770

Jahoda, K., Swank, J. H., Giles, A. B., et al. 1996, in Society of Photo-Optical Instrumentation Engineers (SPIE) Conference Series, Vol. 2808, SPIE, ed. O. H. Siegmund & M. A. Gummin, 59–70

Jain, C., & Paul, B. 2011, Research in Astronomy and Astrophysics, 11, 577, doi: 10.1088/1674-4527/11/5/007

Kaaret, P., Prieskorn, Z., in 't Zand, J. J. M., et al. 2007, ApJL, 657, L97, doi: 10.1086/513270

Kulkarni, A. K., & Romanova, M. M. 2008, MNRAS, 386, 673, doi: 10.1111/j.1365-2966.2008.13094.x

Lamb, F. K., Boutloukos, S., Van Wassenhove, S. o., et al. 2009a, ApJ, 706, 417, doi: 10.1088/0004-637X/706/1/417

—. 2009b, ApJL, 705, L36, doi: 10.1088/0004-637X/705/1/L36

Landau, L. D. 1932, Phys. Zs. Sowjet, 1, 285

Leahy, D. A., Darbro, W., Elsner, R. F., et al. 1983, ApJ, 266, 160, doi: 10.1086/160766

Levine, A. M., Bradt, H., Cui, W., et al. 1996, ApJL, 469, L33, doi: 10.1086/310260

Markwardt, C. B., Strohmayer, T. E., & Swank, J. H. 1999, ApJL, 512, L125, doi: 10.1086/311886

Messenger, C. 2011, Phys. Rev. D, 84, 083003, doi: 10.1103/PhysRevD.84.083003

Messenger, C., & Patruno, A. 2015, ApJ, 806, 261, doi: 10.1088/0004-637X/806/2/261

Middleditch, J., & Kristian, J. 1984, ApJ, 279, 157, doi: 10.1086/161876

Miller, M. C., & Miller, J. M. 2015, PhR, 548, 1, doi: 10.1016/j.physrep.2014.09.003

Muno, M. P., Chakrabarty, D., Galloway, D. K., & Psaltis, D. 2002, ApJ, 580, 1048, doi: 10.1086/343793

Muno, M. P., Fox, D. W., Morgan, E. H., & Bildsten, L. 2000, ApJL, 542, 1016, doi: 10.1086/317031

Özel, F. 2009, ApJ, 691, 1678, doi: 10.1088/0004-637X/691/2/1678

Özel, F., & Freire, P. 2016, ARA&A, 54, 401, doi: 10.1146/annurev-astro-081915-023322

Patruno, A., & Watts, A. L. 2012, arXiv e-prints, arXiv:1206.2727. https://arxiv.org/abs/1206.2727

Patruno, A., Wette, K., & Messenger, C. 2018, ApJ, 859, 112, doi: 10.3847/1538-4357/aabf89

Popham, R., & Sunyaev, R. 2001, ApJ, 547, 355, doi: 10.1086/318336

Ransom, S. M., Eikenberry, S. S., & Middleditch, J. 2002, AJ, 124, 1788, doi: 10.1086/342285

Ransom, S. M., Greenhill, L. J., Herrnstein, J. R., et al. 2001, ApJ, 546, L25, doi: 10.1086/318062

Rothschild, R. E., Blanco, P. R., Gruber, D. E., et al. 1998, ApJ, 496, 538, doi: 10.1086/305377

Shakura, N. I., & Sunyaev, R. A. 1973, A&A, 500, 33

Smith, D. A., Morgan, E. H., & Bradt, H. 1997, ApJL, 479, L137, doi: 10.1086/310604

Strohmayer, T., & Bildsten, L. 2006, New views of thermonuclear bursts, Vol. 39, 113–156

Strohmayer, T. E., & Markwardt, C. B. 2002, ApJL, 577, 337, doi: 10.1086/342152

Strohmayer, T. E., Zhang, W., Swank, J. H., et al. 1996, ApJL, 469, L9, doi: 10.1086/310261

Strohmayer, T. E., Zhang, W., Swank, J. H., White, N. E., & Lapidus, I. 1998, ApJL, 498, L135, doi: 10.1086/311322

Strohmayer, T. E., Arzoumanian, Z., Bogdanov, S., et al. 2018, ApJL, 858, L13, doi: 10.3847/2041-8213/aabf44

Tang, J., Yu, W.-F., & Yan, Z. 2011, Research in Astronomy and Astrophysics, 11, 434, doi: 10.1088/1674-4527/11/4/006

Taylor, J. H., & Weisberg, J. M. 1989, ApJ, 345, 434, doi: 10.1086/167917

Thompson, T. W. J., Rothschild, R. E., Tomsick, J. A., & Marshall, H. L. 2005, ApJL, 634, 1261, doi: 10.1086/497104

Titarchuk, L., Cui, W., & Wood, K. 2002, ApJL, 576, L49, doi: 10.1086/343099

van der Klis, M. 1988, in Timing Neutron Stars, Vol. 262, 27–70

van der Klis, M. 2000, ARA&A, 38, 717, doi: 10.1146/annurev.astro.38.1.717

—. 2006, Rapid X-ray Variability, Vol. 39, 39–112

van der Klis, M., Wijnands, R. A. D., Horne, K., & Chen, W. 1997, ApJL, 481, L97, doi: 10.1086/310656

Villarreal, A. R., & Strohmayer, T. E. 2004, ApJL, 614, L121, doi: 10.1086/425737

Šimon, V. 2012, NewA, 17, 697, doi: 10.1016/j.newast.2012.04.006

Wachter, S., Hoard, D. W., Bailyn, C. D., Corbel, S., & Kaaret, P. 2002, ApJL, 568, 901, doi: 10.1086/339034

Watts, A. L. 2012, ARA&A, 50, 609, doi: 10.1146/annurev-astro-040312-132617

Welsh, W. F., Robinson, E. L., & Young, P. 2000, AJ, 120, 943, doi: 10.1086/301486

Wijnands, R., Strohmayer, T., & Franco, L. M. 2001, ApJL, 549, L71, doi: 10.1086/319128

Wijnands, R., & van der Klis, M. 1998, Nature, 394, 344, doi: 10.1038/28557

Wood, K. S., Ftaclas, C., & Kearney, M. 1988, ApJL, 324, L63, doi: 10.1086/185092

Wood, K. S., Norris, J. P., Hertz, P., et al. 1991, ApJ, 379, 295, doi: 10.1086/170505

Wu, Y. X., Yu, W., Li, T. P., Maccarone, T. J., & Li, X. D. 2010, ApJ, 718, 620, doi: 10.1088/0004-637X/718/2/620

Yu, W., & Yan, Z. 2009, ApJ, 701, 1940, doi: 10.1088/0004-637X/701/2/1940

Zhang, W., Jahoda, K., Kelley, R. L., et al. 1998, ApJL, 495, L9, doi: 10.1086/311210